Analysis and design of recycled glass bead sandwich panels in bending

Finian McCann[1*]

School of the Built Environment and Architecture, London South Bank University, 103 Borough Road, London, UK

[1]mccannf@lsbu.ac.uk; * corresponding author

Abstract

The bending resistance of recycled glass bead sandwich panels is investigated through flexural experiments conducted on a range of specimens. A method whereby the maximum strains at midspan are used to determine the elastic material properties is discussed and shown to provide similar results to a method based on midspan deflections; scopes of applicability of the two methods are discussed. The influences of adhesive strength, polymer content and previous damage are investigated, with the application of high-strength adhesive not leading to any improvement in structural performance whereas the increase in polymer content is shown to improve structural performance. Re-testing of previously damaged specimens demonstrates that residual compaction in the core leads to improved deformation capacity. A strain-based model to predict the ultimate moment resistance is shown to provide safe-sided results when compared to the experimental ultimate moments. A reliability analysis of the predictive model is conducted in accordance with the European structural design framework. For 1–2 mm bead cores, a partial factor of 1.40 is recommended for use with the design method, while a partial factor of 2.20 is recommended for 4–8 mm bead cores; it is confirmed that the design moment resistances are conservative and safe-sided when compared to the experimental results.

1. Introduction

Composite sandwich panels are finding increasing use in structural contexts in response to growing demand for prefabricated construction and offsite manufacturing methods that reduce the time, cost and labour expended on structural assembly [1,2]. Composite sandwich panels combine stiff outer facing sheets that usually provide the majority of the flexural rigidity with a lightweight core that usually provides other functions such as thermal insulation, acoustic insulation, energy absorption, fire resistance or structural depth to aid deflection limitation [3–5]. Having originally found use in the field of aeronautics where weight optimisation is paramount [3], materials used in structural sandwich panels include metal facing plates [6], precast concrete [7], timber [8], fibre-reinforced polymers [9], metallic honeycombs [10] and metallic foams [11,12].

The present study concerns recycled glass bead sandwich panels (RGBSPs) comprising two fibreglass facing sheets surrounding an inner core of recycled glass beads bonded by a polymer resin, as shown in Figure 1a. RGBSPs have been available commercially for a number of years [13] and can potentially be used as floor panels, wall panels, roofing elements, cladding panels, fire barriers and stand-alone acoustic barriers [13,14]. The bead core can be considered as a type of glass-polymer composite, with glass fibre–reinforced polymers (GFRPs) being the most prominent examples of the use of such materials in construction [15]. When considering particulate glass as opposed to glass fibres, the inclusion of recycled glass in construction materials has a number of precedents, including in concrete and cement mortar [16,17], in asphalt [18,19] and in masonry [20]. These studies have demonstrated that the structural performance of materials containing glass beads is at least as effective as that of conventional analogues. In addition, since it is common that mixed forms of waste glass vary considerably in their chemical compositions and are thus not suitable for reforming [17], the use of waste glass in construction materials offers a more convenient route for repurposing such materials. The environmental resilience of glass [21] and polymer [22]

materials serve to increase the longevity of RGBSPs in construction, thus also enhancing sustainability. The polymer content of RGBSP cores is typically 6–8% by volume, with the polymer acting as a binding agent between the glass beads while also entrapping a notable volume of air voids as shown in Figure 1b. These voids reduce vibrations [23], enhance acoustic insulating performance [14] and improve thermal insulation efficiency during the operational lifespan of a building structure [13]. The low specific weight (approximately 4.2 kN/m^3 [14]) and portability of RGBSPs make them ideally suited to applications in modular construction, where whole units can be fabricated offsite and transported to their final location. Alternatively, the panels can be easily manipulated onsite, making them also well-suited for temporary applications such as emergency shelters or as temporary noise barriers.

The panels investigated in the present study are fabricated on an industrial scale by initially coating beads formed from recycled glass in a thermoset polymer resin in order to bind the core together. Differing material properties can be achieved through control of the size of the glass beads and through specification of the polymer volume fraction. Prior to their inclusion in the core mix, glass bead fragments are sieved in order to sort them into ranges of 0–1 mm, 1–2 mm, 2–4 mm and 4–8 mm. After mixing, the resultant core is formed to the required dimensions and passed through an extruder. An epoxy-based adhesive is applied to two fibreglass facing sheets which are then pressed mechanically on to either side of the core. Given that the manufacturing process is not overly complicated and that the main constituent material, i.e., recycled glass, is relatively inexpensive to source, RGBSPs thus offer a cost-effective and environmentally sustainable solution to meet the increasing demands of the construction industry.

The governing failure mode of a sandwich panel in bending is influenced by the relative strengths and stiffnesses of the facing sheets, the core and the bonding agent between them, as well as the geometric dimensions. In the case of panels containing highly-compressible foam cores, the failure mode in bending tends to involve either wrinkling of the facing sheets [24] (see Figure 2a), an interaction between global buckling and facing sheet wrinkling [25] or indentation [26]; however, the brittle nature of recycled glass bead cores precludes such modes. If the shear strength of the adhesive is less than or similar to the strength of the facing sheet or core materials then delamination (see Figure 2b) is also possible [27,28] – the resulting loss of shear connectivity between the facing sheet and the core can precipitate an overall loss of stability and structural performance of the panel [29]. In cases such as RGBSPs where the core is weaker and more brittle than the facing sheets and the adhesive, the mode of failure tends to be due to shear within the core (see Figure 2c).

The mechanical properties and failure modes of particulate-polymer composites such as the bead core are influenced by the size of the particles, the particle volume fraction and the interfacial adhesion between the particles and the polymer matrix [30,31]. At the microscale, the failure mode within particulate-polymer composites involves either interfacial debonding between the glass beads and the polymer (see Figure 3 [32]) or breakage of the particles [33]. Because of their low polymer content compared to conventional particle-reinforced polymers, RGBSPs tend to experience a brittle mode of failure within the core while the fibreglass facing sheets maintain their integrity, with delamination of the facing sheets from the core rarely being the primary mode of failure. Previous testing of RGBSPs in bending [14] found that the elastic stiffness was higher in cores containing smaller glass beads, although the strength was not influenced significantly by the glass bead size; it was also found that the deformation capacity was higher in cores containing larger glass beads. These trends are in keeping with the findings of previous studies of glass-polymer composites [30–33].

Through a combination of flexural testing of small-scale specimens and bend testing of full-scale panels, the present study expands upon previous results [14] for the bending resistance of RGBSPs. In particular, the influence of polymer content, adhesive strength and previous damage, which is

important when considering structural robustness, on load and deformation capacity are examined. The material behaviour of the bead core is described in detail through analysis of the strain distribution at the mid-span cross-section during the experiments. The measured strain distributions are used to inform a strain-based method for predicting the midspan bending moment; this model is then adapted to predict the ultimate moment resistance of a panel in bending. Finally, reliability analyses conducted in accordance with EN 1990 [34] to calibrate material partial factors of safety for the design of RGBSPs in bending are described. The definition of an appropriate partial factor thus allows for the safe design of RGBSPs in accordance with the principles of structural reliability enshrined in the European structural design framework.

2. Experiments

A series of flexural tests on small-scale specimens and bending tests of full-scale RGBSP specimens have been conducted in the Strengths of Materials laboratory at London South Bank University. In this section, the experimental methodologies are described and the results for elastic mechanical properties, the load–deflection behaviour, failure modes and bending strain distributions are discussed.

2.1 Flexural testing of small-scale panel sections

Flexural tests have been conducted on small-scale panel sections using the Tinius Olsen H25 KS universal testing machine shown in Figure 4a. Three specimens, labelled F01, F02 and F03, were cut from RGBSPs with 1–2 mm glass bead cores, with each specimen having a nominal length L_{nom} = 300 mm, a nominal overall depth h = 54 mm and a nominal breadth b = 50 mm; average measured values of these properties as well as the average thicknesses of the layer of fibreglass t_{fg} are shown in Table 1. As indicated in Figure 4b, the specimen is loaded in four-point bending with the span between the supports L = 240 mm and the point loads positioned at third points, i.e., the distance between a support and its adjacent point load a = 80 mm. A linear variable displacement transducer (LVDT) is positioned underneath the specimen at midspan in order to record the vertical deflection while the internal load cell records the total applied load P. Strain gauges are attached at the top and bottom outer surfaces of the fibreglass sheets at midspan in order to measure longitudinal strains at the extreme fibres of the cross-section. The specimens are loaded monotonically without pause to failure under displacement control at a rate of 0.15 mm/min. Graphs of P against the vertical deflection at midspan δ for the three specimens are shown in Figure 5. Although it can be seen that there exists a degree of variability between their flexural responses, after a certain amount of deformation (δ = 0.5–0.6 mm), the material undergoes some softening with the flexural rigidity of the specimens reducing up until failure. From a micromechanical perspective, analogies can be drawn from analyses of fibre-ceramic composites in tension [35,36], whereby the constituent materials of the glass-polymer composite initially undergo elastic deformation up to a level of strain whereupon damage at the microscale initiates that manifests itself at the macroscale as an overall loss of stiffness; the damage mechanisms include cracking of the polymer matrix and interfacial debonding from the particles [32,33]. Damage continues to propagate through the specimen with increasing load until failure occurs, with a large diagonal crack such as that shown in Figure 4a visible.

In accordance with Euler–Bernoulli beam theory, it is assumed that the longitudinal strains arising from bending vary linearly with depth through the cross-section as shown in Figure 6; thus, the maximum compressive and tensile strains in the bead core, $\varepsilon_{c,c}$ and $\varepsilon_{c,t}$, respectively, are slightly reduced when compared to the compressive and tensile strains, ε_{comp} and ε_{tens}, measured at the top and bottom strain gauges, respectively, at midspan. It should be noted that the absolute value of the compressive strain is referenced throughout the present study. In Figure 7, the applied load P is plotted against the maximum compressive and tensile strains in the bead core $\varepsilon_{c,c}$ and $\varepsilon_{c,t}$ for the

three flexural test specimens. It can be seen that, when testing specimens F01 and F02, the compressive and tensile strains are almost identical up to strains of 0.153% and 0.151%, respectively; in the case of specimen F03, the discrepancy is apparent at a lower level of strain. The implications of these discrepancies are clearer upon examination of the graphs of the strain ratio ε_{comp} / ε_{tens} against $\varepsilon_{c,t}$ shown in Figure 8. For specimens F01 and F02, the strain ratio is initially approximately equal to unity – this initially balanced behaviour suggests that the tensile and compressive responses of the material are equivalent. Assuming linearly-varying strains, a strain ratio of ε_{comp} / ε_{tens} = 1 implies a symmetric strain distribution like that shown in Figure 6a where the neutral axis of bending passes through the geometric centre of the composite cross-section. Once the limiting elastic strain of the bead core material $\varepsilon_{c,el}$ is exceeded, softening initiates within the material on the tension side; this is evidenced by ε_{tens} increasing at a greater rate than ε_{comp} in Figure 7 and the strain ratio decreasing in Figure 8. These observations suggest that the bead core material is weaker in tension than it is in compression. If the material on the tension side of the specimen has softened and lost efficacy then there must be an associated change to the neutral axis of bending. The strain distribution associated with ε_{comp} / ε_{tens} < 1 is shown in Figure 6b, where the neutral axis of bending has shifted towards the top (compression) face of the section. The upwards shift of the neutral axis Δ_{NA} is given thus:

$$\Delta_{NA} = \left(\frac{\varepsilon_{tens} - \varepsilon_{comp}}{\varepsilon_{tens} + \varepsilon_{comp}}\right)\left(\frac{h}{2}\right) \tag{1}$$

Taking this shift in the neutral axis into account, values for $\varepsilon_{c,c}$ and $\varepsilon_{c,t}$ are given by:

$$\varepsilon_{c,c} = \varepsilon_{comp}\left(\frac{\frac{h_c}{2} - \Delta_{NA}}{\frac{h}{2} - \Delta_{NA}}\right) \tag{2a}$$

$$\varepsilon_{c,t} = \varepsilon_{tens}\left(\frac{\frac{h_c}{2} + \Delta_{NA}}{\frac{h}{2} + \Delta_{NA}}\right) \tag{2b}$$

In Figure 8, the strain ratio for specimen F03 is initially approximately equal to 0.90, which is anomalous when compared to the balanced behaviour observed in specimens F01 and F02, and also the undamaged full-scale panels discussed in Section 2.2. The strain ratio remains relatively constant at this value up to a value of $\varepsilon_{c,t}$ = 0.146%, whereupon the material on the tension side softens and the strain ratio decreases. The lower initial strain ratio is thought to be the consequence of a thicker layer of adhesive being applied on the compression side in addition to misalignments when positioning the specimen and the strain gauges. Applying Eq.(1), it appears that, initially, the neutral axis of bending of specimen F03 does not pass through the geometric centre but is located 1.43 mm towards the compression side.

In each of the flexural specimens tested, cracks can be seen to originate on the tension side of the specimen after softening has occurred, which are caused by interfacial debonding between the glass beads and the polymer. As failure is approached, a large diagonal crack such as that shown in Figure 4a is seen to propagate from the tension side up towards the compression face of the specimen – this diagonal pattern is a result of the interaction between bending stresses, shear stresses and local bearing stresses above the supports and underneath the point loads. Eventually at a value of $\varepsilon_{c,t}$ = 0.45–0.50% the crack has propagated throughout the entire specimen and failure occurs.

2.1.1 Determination of mechanical properties

Previous estimates [14] for the elastic flexural modulus of the bead core material $E_{c,f}$ were determined through comparison of the experimental midspan deflection and the predictions of Euler–Bernoulli beam theory, which assumes that shear strains are negligible and thus that vertical deflections arise purely as a consequence of bending curvature. However, when considering the relatively short and stocky flexural specimens examined in the present study, the shear and bearing stresses developed during loading contribute towards a significant portion of the vertical deflections in the specimens. Thus, values for $E_{c,f}$ that are determined based on the midspan deflection are underestimated since Euler–Bernoulli beam theory assumes that the development of deflections across the specimen is wholly, rather than partially, attributed to bending curvature. For the full-scale beam specimens, the contribution of shear and bearing stresses is proportionally less and therefore estimates arrived at through analysis of the deflection at midspan are more accurate.

For the flexural specimens examined in the present study, the longitudinal strains recorded at midspan are used to estimate $E_{c,f}$. Since shear stresses and bearing stresses are negligible at midspan in a four-point bending configuration, it can be assumed that strains arising at the extreme fibres can indeed be wholly attributed to bending. Assuming that the longitudinal strains vary linearly with depth through the cross-section as shown in Figure 10, the moment M predicted at midspan in accordance with Euler–Bernoulli beam theory is:

$$M = \frac{(\varepsilon_{\text{tens}} + \varepsilon_{\text{comp}})(EI)_{\text{eff}}}{h} \tag{3}$$

where $(EI)_{\text{eff}}$ is the effective flexural rigidity of the composite section:

$$(EI)_{\text{eff}} = E_{\text{fg}} I_{\text{fg}} + E_{\text{c,f}} I_{\text{c}} \tag{4}$$

and $I_c = bh_c^3/12 + bh_c\Delta_{NA}^2$ and $I_{fg} = b(h^3 - h_c^3)/12 + 2bt_{fg}\Delta_{NA}^2$ are the second moments of area of the bead core and fibreglass sheets, respectively, about the neutral axis of bending that incorporate any shifts from the geometric centre of the composite cross-section. The elastic modulus of the fibreglass sheet E_{fg} is taken to be 7589 N/mm^2 [14]. It should be noted that the validity of Eqs.(3) and (4) prevails only while the responses of the material in tension and compression are equivalent; once the limiting elastic strain $\varepsilon_{c,el}$ is exceeded and the material on the tension side begins to soften, the flexural rigidity of the bead core requires more detailed calculation. However, for tensile strains less than $\varepsilon_{c,el}$, Eqs.(3) and (4) can be manipulated to determine $E_{c,f}$, with the bending moment at midspan $M = Pa/2$ substituted into Eq.(3). With the flexural modulus known, the limiting elastic strength of the bead core is given by:

$$\sigma_{c,el} = E_{c,f}\, \varepsilon_{c,el} \tag{5}$$

The results obtained from the flexural tests for $E_{c,f}$, $\varepsilon_{c,el}$ and $\sigma_{c,el}$ are shown in Table 1. In the present study, values of $\varepsilon_{c,el}$ are defined as the value of $\varepsilon_{c,t}$ when ε_{comp} / ε_{tens} drops below 95% of its initial value. It is noted that the average value of $E_{c,f}$ = 1201 N/mm^2 agrees well with the average elastic modulus of 1–2 mm glass bead cores of 1126 N/mm^2 based on analysis of midspan deflections [14]. Previous estimates for the average values of $\varepsilon_{c,el}$ and $\sigma_{c,el}$ of 0.135% and 1.45 N/mm^2 are somewhat reduced compared to the values of 0.150% and 1.80 N/mm^2, respectively, found in the present study. Comparison of $\sigma_{c,el}$ with the compressive strength of the bead core $\sigma_{c,c}$ of approximately 2.1 N/mm^2 [14] confirms that that the material is indeed weaker in tension. It is noted that the limiting elastic strains found for the bead cores in the present study are approximately equivalent to those found for ceramic matrix minicomposites employed in aeronautical applications [35,36].

2.2 Bend testing of full-scale panels

In this section, four-point bending tests conducted on full RGBSP specimens are discussed. The experimental methodology is described and results for the load–deflection behaviour, failure modes and elastic material properties are presented. The influence of a number of parameters are discussed, including the strength of the adhesive between the fibreglass and bead core, the polymer binder content of the bead core, and previous damage to the specimens; where applicable, comparisons are made with control samples tested previously [14].

The nominal dimensions and glass bead diameters of the specimens examined are shown in Table 2. In total, twelve specimens were tested as part of the present study with eight specimens from [14] being used as control specimens. The specimens are labelled in the following manner: P[specimen number]-[minimum glass bead diameter in mm]-B[nominal panel breadth in mm]-L[nominal span between supports in mm]-[specialisation suffix]. The specialisation suffixes are defined in order to discriminate between panels with high-strength adhesive (HSA), panels with increased polymer binder content in the bead core (XB), and panels extracted from previously-damaged test specimens (DM). For example, specimen P19-1-B150-L1650-HSA is a 150 mm-wide beam spanning 1650 mm between supports with the fibreglass sheets attached using high-strength adhesive to a core containing glass beads 1–2 mm in diameter.

2.2.1 Methodology

The bending tests were conducted using the loading rig shown in Figure 9, which comprises a 2.5 m-long steel I-section support beam secured into 250 kN Zwick/Roell universal testing machine, roller supports, a spreader bar atop half-round contacts at the loading points, an LVDT positioned underneath the specimen at midspan, and a data acquisition system; strain gauges were also affixed to the top and bottom surfaces of specimens P25–P28 at midspan. In order to accommodate some rotation at the ends of the beams, overhangs are provided at the ends of the specimens, resulting in the tested spans L being somewhat shorter than the overall length L_{nom} of the specimens as shown in Table 2. The specimens are loaded monotonically without pause under displacement control at a crosshead displacement rate of 5 mm/min until failure.

Estimates for the elastic properties $E_{\text{c,f}}$, $\varepsilon_{\text{c,el}}$ and $\sigma_{\text{c,el}}$ are found through analysis of the midspan deflections measured by the LVDT. The effective flexural rigidity of the composite cross-section $(EI)_{\text{eff}}$ is found by manipulating the expression, according to Euler–Bernoulli beam theory, for the vertical deflection at midspan of a beam loaded in four-point bending with loads $P/2$ positioned a distance a from their closest support (as indicated in Figure 4b):

$$(EI)_{\text{eff}} = \frac{a}{48}(3L^2 - 4a^2)\left(\frac{\Delta P}{\Delta \delta}\right) \tag{6}$$

where $\Delta P/\Delta\delta$ is the gradient of the load–midspan deflection curve calculated using the measured values of the total applied load P and the vertical deflection at midspan δ. In order to counteract noise in the experimental values, moving averages of $\Delta P/\Delta\delta$ taken over a displacement interval of 0.25 mm are used. In Figure 10a, a typical graph of $\Delta P/\Delta\delta$ against δ is shown for the example of specimen P20. It can be seen that there is an initial regime where the gradient is approximately constant, followed by a decrease in flexural rigidity, followed by a final regime where the gradient is approximately constant again. Analogous micromechanical analysis of fibre-matrix composites [35,36], where similar behaviour is observed, has shown that these regimes reflect, respectively: i) initial linear elastic deformation of the particles and matrix, ii) damage occurring at the microscale within the composite such as matrix cracking and partial interfacial debonding, and iii) fracture of the matrix and more complete interfacial debonding leading to cracks visible at the macroscale. Although the overall mode of failure primarily involves diagonal shear-induced cracking like that shown in Figure 4a, prior to failure, cracks are also observed to propagate directly upwards from

the tension-side facing sheet across the central segment of the panel where the bending moment is at a maximum; the fibreglass facing sheets serve to reinforce the core so that stresses within it can be redistributed around the cracks. Upon comparison with the corresponding graph of P against δ shown in Figure 10b, it can be seen the regimes correspond to initial linear behaviour, nonlinear softening and linear behaviour but with reduced stiffness, respectively; identification of the ranges of these regimes is facilitated considerably through examination of the gradient–displacement curve rather than the load–displacement curve. Considering the initial linear elastic regime where $\Delta P/\Delta\delta$ is approximately constant, $(EI)_{\text{eff}}$ is calculated using the average value of $\Delta P/\Delta\delta$ up to when softening initiates. With $(EI)_{\text{eff}}$ known, Eq.(4) can then be manipulated to estimate $E_{\text{c,f}}$. The limiting elastic strain $\varepsilon_{\text{c,el}}$ is defined as the maximum tensile strain in the bead core at the point when $\Delta P/\Delta\delta$ falls below 95% of its initial value; the maximum strain in the bead core $\varepsilon_{\text{c,t}}$ is given by:

$$\varepsilon_{\text{c,t}} = \frac{1}{4} P a h_{\text{c}} \, (EI)_{\text{eff}} \tag{7}$$

It should be noted that the use of Eq.(4) in conjunction with Eqs.(6) and (7) assumes that the neutral axis of bending is collinear with the major cross-sectional axis, i.e., that $\Delta_{\text{NA}} = 0$ and the compressive and tensile strains are equivalent. With $\varepsilon_{\text{c,el}}$ known, the elastic strength of the bead core material $\sigma_{\text{c,el}}$ can be found through application of Eq.(5).

2.2.2 Structural behaviour

In this section, the results of the bending tests are discussed, with comparisons made to relevant control specimens where applicable, including the load–deflection relationships, the failure modes, the ultimate moments, the deflections at ultimate load and the elastic mechanical properties. In particular, the influences of high-strength adhesive, increased polymer content and previous damage are investigated.

Values of the ultimate moment per unit width M_{u} / b are plotted against δ_{u} / L^3 in Figure 11, where $M_{\text{u}} = P_{\text{u}} a/2$ and δ_{u} is the vertical midspan deflection at the ultimate load P_{u}. Since all the specimens were loaded with point loads in four-point bending, values of δ_{u} / L^3 are calculated in order to provide a comparable measure of deformation capacity between members of varying spans; values of M_{u} / b provide a comparable measure of load capacity between panels of varying widths. In order to provide some context, the characteristic moment resistance of a 150 mm-deep C30 concrete slab reinforced with 12 mm H500 bars at 300 mm centres is approximately 21 kNm/m; when considering that RGBSPs have a unit weight of approximately 4.2 kN/m^3 [14], the specimens included in Figure 11 are thus capable of rivalling the moment resistance of typical reinforced concrete flooring systems while being almost six times less dense.

2.2.2.1 Elastic properties

The values of $E_{\text{c,f}}$, $\varepsilon_{\text{c,el}}$ and $\sigma_{\text{c,el}}$ of the bead cores, which have been determined using the midspan deflection method, are shown in Table 3. Values of $E_{\text{c,f}}$ are shown in Figure 12 while values of $\varepsilon_{\text{c,el}}$ and $\sigma_{\text{c,el}}$ are shown in Figure 13. In Figure 12, it can be seen that neither the inclusion of the high-strength adhesive nor the additional polymer binder has led to an appreciable increase in $E_{\text{c,f}}$, while the elastic modulus of the damaged specimens has decreased considerably as would be expected. Similarly, it can be seen in Figure 13 that neither the inclusion of the high-strength adhesive nor the additional polymer has led to a significant increase in $\sigma_{\text{c,el}}$; the benefit of the additional binder lies in the increase to the ultimate resistance of the panels shown in Figure 11. The values of $\varepsilon_{\text{c,el}}$ for specimens P17 to P24 and specimens P27 and P28 lie approximately within the same range as the

control specimens; as is also indicated in Figure 11, the ductility of the damaged specimens P25 and P26 is noticeably enhanced when compared to their parent beams, albeit with the strength being somewhat reduced.

2.2.2.2 Influence of high-strength adhesive

Load–deflection relationships are shown in Figure 14 for specimens P17 to P20 containing a high-strength epoxy-based adhesive; comparison is made with the control specimens P07 to P10. It can be seen that there is little difference between their respective responses, with the inclusion of the high-strength adhesive not affecting the ultimate resistance and only marginally increasing deformation capacity (see also Figure 11). The limiting elastic strain of the control specimens is marginally higher than that of the specimens tested in the present study as evidenced by the deflection at which the flexural rigidity begins to decrease being greater. The cause of these similarities can be explained upon examination of the failure modes shown in Figure 15 (which are typical for the majority of specimens tested): the interfacial bonds between the polymer and the glass beads within the core are weaker than either of the normal or high grade adhesives, and so the core cracks along a layer above the adhesive rather than any delamination occurring. Thus, increasing the adhesive strength has little to no influence on the overall resistance or rigidity of the specimens. Some delamination can be observed on the top (compression) side of the specimens shown in Figure 15, which occurs after the attainment of the ultimate load; post-failure compression-side delamination was observed to occur in a number of tests but very rarely was it the initiating mechanism of failure.

2.2.2.3 Influence of increased polymer content

Load–deflection relationships for specimens P21 to P24 with a core polymer content greater than the usual 7% by volume are shown in Figure 16. In keeping with Figure 11, it can be seen that there is a significant improvement to both the ultimate resistance and deformation capacity when compared to the performances of the control specimens (P11 to P14): the average moment resistance is 23% higher while the average deformation capacity is 34% higher. The increased polymer content improves the bonding between the glass beads and thus allows for a greater degree of stress transfer through the core. While the exact increased polymer volume fraction is commercially sensitive, it can be assumed that the relative increases in performance do not match the increase in binder with total efficiency, such that the relative increase in binder is indeed in excess of 34%. The failure modes observed in these specimens are overall similar to that shown in Figure 15; however, upon examination of the failure mode shown in Figure 17 for specimen P22, it can be seen that delamination of the facing sheet from the bead core has occurred on the tension side, i.e., it is the adhesive that has failed rather than cracking propagating through the bead core. This can be attributed to the additional polymer increasing the ultimate strength of the bead core such that it is similar to or greater than that of the adhesive.

2.2.2.4 Influence of previous damage

In Figure 18, graphs of applied moment M against δ / L^3 are shown for the previously-damaged specimens (P25 and P26), which were cut from the ends of two specimens with increased binder content (P21 and P23, respectively); these ordinates have been plotted in the graphs instead of the load and midspan deflection in order to account for the differing spans. Although the ultimate resistances of the damaged specimens are certainly lower than those of the original specimens, it is clear that the deformation capacity has increased considerably (as is also suggested by Figure 11). This phenomenon can be explained by noting that specimens P25 and P26 were turned over after being cut from their parent specimens so that the side that was originally in compression was re-tested in tension, and vice versa. During the retests, there is thus a pre-existing degree of compressive plastic deformation (compaction) on the tension side that must be reversed before

tensile deformation is experienced, resulting in the enhanced deformation capacity observed. Conversely, any cracks that were pre-existing on the tension side are now re-closed in compression, thus limiting the propagation of cracking. This is encouraging evidence that pre-compression of RGBSPs has the potential to increase their load and deformation capacities, thus allowing for longer spans to be achieved; the principle is analogous to the pre-stressing of concrete.

2.2.3 Strain distributions

In order to inform an accurate representation of bending strain distributions through the bead core, specimens P25 to P28 were fitted with strain gauges on their top and bottom faces at midspan. The load–deflection curves for specimens P27 and P28 are shown in Figure 19. In keeping with previous findings, specimen P27 (containing the 1–2 mm bead core) has a slightly higher initial linear stiffness and softens at a slightly larger deflection than specimen P28 (containing the 4–8 mm bead core). Somewhat anomalously, a sudden loss of load-carrying capacity occurred at P = 19.2 kN during testing of specimen P27, equivalent to a distributed ultimate moment M_u / b of 16.0 kNm/m, whereas P28 failed at 30.2 kN, equivalent to M_u / b = 25.2 kNm/m, which is more in keeping with other observations as shown in Figure 11. Upon examination of the failure mode shown in Figure 20a, it can be seen that, in conjunction with the typical diagonal crack propagating from the tension side, clear delamination of the compression-side fibreglass sheet has also occurred – usually, some glass bead remains adhered to the inside of the facing sheet. It can be seen in Figure 20b that specimen P28 has failed in a more typical fashion, with tension-side cracking visible above the fibreglass sheet culminating in a diagonal crack propagating towards the compression side, similar to the failure modes shown in Figure 15. As indicated in Figure 20a, inspection of specimen P27 after testing suggests that some damage or deterioration had been incurred before the tests that affected its performance; the anomalously low moment resistance of specimen P27 is obvious upon examination of the values of M_u / b in Figure 11.

Graphs of the maximum compressive and tensile strains in the bead core $\varepsilon_{c,c}$ and $\varepsilon_{c,t}$ are shown in Figure 21 for specimens P25 to P28. Similar to the behaviour observed in the flexural specimens discussed in Section 2.2, in specimens P27 and P28 (see Figure 21c–d), the tensile and compressive strains are equivalent up to a particular level of strain. In the case of the previously-damaged specimens P25 and P26 (see Figure 21a–b), it is apparent that the material is initially more stiff on the tension side, more noticeably so in specimen P25; after a certain amount of strain, the material on the tension side softens and becomes less stiff in keeping with other observations. The initially stiffer response of the tension-side material is evidence of residual compression-side compaction from the original tests conducted on specimens P21 and P23 that must be reversed before tensile softening can occur.

Comparing panel specimens P27 and P28 (see Figure 21c–d), it can be seen that, in keeping with the findings of [14], softening initiates at a relatively lower strain in specimen P28 with the 4–8 mm core than it does in specimen P27 with the 1–2 mm bead core. As shown in Figure 21d, the overall stiffness of specimen P28 decreases continuously until failure occurs at P = 30.2 kN; however, in the case of specimen P27, it can be seen that at P = 19.2 kN, the compressive strain ceases to increase smoothly and reverses abruptly – this is evidence of a sudden slip occurring in the proximity of the strain gauge, i.e., the failure of the adhesive on the compression side leading to the delamination visible in Figure 20a. It should be noted that no other beam or panel tested in the present study or previously [14] suffered an early-onset compression-side failure such as this; in a small number of specimens, compression-side delamination was observed to occur only after the typical propagation of tension-side cracks had precipitated failure (see Figure 15). It can be seen that the tensile strain continues to increase after the slip occurred, with an eventual terminal loss of load-carrying capacity occurring at P = 16.9 kN. As noted by [29], delamination leads to a local loss of stiffness and hence destabilisation of the overall panel, such that the ultimate resistance can be considerably reduced;

the loss of stability is evidenced by the sudden drops in load-carrying capacity shown in Figure 19 for specimen P27.

Applying the approach described in Section 2.1 for the flexural specimens, the onset of softening is defined through examination of the ratio of measured compressive to tensile strains ε_{comp} / ε_{tens}, graphs of which are plotted against the maximum tensile strain in the bead core $\varepsilon_{c,t}$ in Figure 22. It can be seen that the curves for specimens P27 and P28 are initially constant and fall below 95% of their initial values at values of $\varepsilon_{c,t}$ of 0.107% and 0.094%, respectively. The tensile strains at failure of specimens P27 and P28 are 0.690% and 0.902%, respectively, although it is surmised that a higher tensile failure strain for the bead core of specimen P27 would have been recorded had the specimen not failed prematurely. In the case of the previously-damaged specimens P25 and P26, the curves are initially more rounded and thus the point of the onset of softening is less clear; taking the onset of softening as the point where ε_{comp} / ε_{tens} falls below 95% of its initial value, values of $\varepsilon_{c,t}$ equal to 0.155% and 0.124% are found for specimens P25 and P26, respectively.

Values of $E_{c,f}$ for specimens P25 to P28 found using the midspan strain method are shown in Table 4, with comparison made to values found using the midspan deflection method. It is reiterated that use of the midspan deflection method is likely to underestimate the value of $E_{c,f}$ because it neglects the shear strains and strains arising from direct bearing that also contribute to the deflection at midspan. In the case of specimens P25 to P27, it is apparent that the pre-existing damage to the specimens has precipitated further localised decreases in stiffness, leading to a greater discrepancy between the results of the two methods; it should also be noted that the midspan deflection method assumes that the neutral axis initially passes through the geometric centre of the cross-section, which is not the case for specimens P25 and P26 upon inspection of Figure 22 since ε_{comp} / ε_{tens} > 1.0. It is noted that such discrepancies can occur when estimating elastic moduli of other particulate composite materials like concrete, where differing models [37,38] can return estimates for the elastic modulus of the same grade of concrete that vary by upwards of 16%. It is preferable that values for $E_{c,f}$ found using the midspan strain method be used where available since this method is less prone to the influence of shear and bearing stresses, and gives a more accurate representation of the stiffness of the material in pure bending. Values of $E_{c,f}$ found using the midspan deflection method are more conservative and lead to safe-sided designs but should only be derived from tests conducted on long-spanning beams (L/h > 8) where the influence of shear and bearing stresses will not overly affect the estimation of $E_{c,f}$.

3. Design of recycled glass bead sandwich panels in bending

In this section, the results of the bending tests are used to inform a strain-based method for determining the bending moment in an RGBSP. Comparisons are made between the predictive model and the experimental results for applied moment. With the model validated satisfactorily it is then adapted to predict the ultimate moment resistance of a panel in bending. A reliability analysis is conducted in accordance with EN 1990 [34] in order to determine an appropriate partial factor of safety for use with the predictions of the model when designing RGBSPs in bending.

3.1 Strain-based model for bending moment

In Section 2, it is seen how strain measurements taken at midspan can be used to identify changes in the material behaviour of the glass bead cores and to estimate elastic material properties. In order to predict the behaviour of an RGBSP when the bead core is undergoing plastic deformation at strains in excess of $\varepsilon_{c,el}$, it is assumed conservatively that the core behaves in a perfectly-plastic manner with no strain hardening up to a tensile strain at failure $\varepsilon_{c,tf}$ (see Figure 23); since the

compressive strength of the bead core $\sigma_{c,c}$ is greater than its tensile strength $\sigma_{c,el}$, it is not necessary to define a compressive failure strain explicitly for this analysis. Since the strength of the fibreglass sheet is approximately 200 N/mm^2 [39] and thus greatly exceeds that of the bead core, it is assumed that the facing sheets remain elastic throughout the entire loading regime and thus the moment contribution of the facing sheets is dependent upon the level of strain.

The strain and stress distributions arising in a cross-section of an RGBSP in bending undergoing plastic deformation are shown in Figure 24. The material on the tension side is elastic down to a distance from the neutral axis equal to y_t while the material on the compression side is elastic up to a distance from the neutral axis equal to y_c; the material is assumed to undergo plastic deformation beyond these distances from the neutral axis, with the stress on the tension side equal to the limiting elastic strength $\sigma_{c,el} = \varepsilon_{c,el}E_{c,f}$ and the stress on the compression side assumed to the equal to the compressive strength of the bead core $\sigma_{c,c}$. The distances y_t and y_c are given by:

$$y_t = \frac{\sigma_{c,el}}{\varepsilon_{tens}E_{c,f}}\left(\frac{h}{2} + \Delta_{NA}\right) \leq \frac{h_c}{2} \tag{8a}$$

$$y_c = \frac{\sigma_{c,c}}{\varepsilon_{comp}E_{c,f}}\left(\frac{h}{2} - \Delta_{NA}\right) \leq \frac{h_c}{2} \tag{8b}$$

The moment M acting at the cross-section can be found by integrating the infinitesimal moments $dM = b\sigma(y)y\,dy$ across the depth of the section, where y is the vertical distance from the neutral axis to an element of the cross-section of thickness dy and $\sigma(y)$ is the bending stress acting on the element. Assuming the stress blocks shown in Figure 24, the expression for M is:

$$M = b\left(\int_{-\left(\frac{h}{2}+\Delta_{NA}\right)}^{\frac{h}{2}-\Delta_{NA}} \sigma(y)\, y\, dy\right) = M_{fg} + M_{c,el} + M_{c,pl} \tag{9}$$

where the moment contribution of the fibreglass sheets M_{fg}, the elastic moment contribution of the bead core $M_{c,el}$ and the plastic moment contribution of the bead core $M_{c,pl}$ are given by, respectively:

$$M_{fg} = bE_{fg}\left(\frac{\varepsilon_{comp} + \varepsilon_{tens}}{h}\right)\left(\frac{h^3}{12} - \frac{h_c^3}{12} + (h - h_c)\Delta_{NA}^2\right) = E_{fg}\left(\frac{\varepsilon_{comp} + \varepsilon_{tens}}{h}\right)I_{fg}$$

$$M_{c,el} = \frac{1}{3}bE_{c,f}\left(\frac{\varepsilon_{comp} + \varepsilon_{tens}}{h}\right)(y_c^3 + y_t^3)$$

$$M_{c,pl} = \frac{b}{2}\left(\sigma_{c,c}\left(\left(\frac{h_c}{2} - \Delta_{NA}\right)^2 - y_c^2\right) + \sigma_{c,el}\left(\left(\frac{h_c}{2} + \Delta_{NA}\right)^2 - y_t^2\right)\right)$$

It is noted that the expression for M_{fg} includes the second moment of area of the fibreglass sheets relative to the shifted neutral axis of bending $I_{fg} = b(h^3 - h_c^3)/12 + b(h - h_c)\Delta_{NA}^2$. The accuracy of the model is assessed by comparing the predictions of Eq.(9) with the experimental applied moment $Pa/2$. In Figure 25, graphs of moment against the vertical deflection at midspan are shown for specimens P25 to P28. The predicted bending moments that are plotted against the vertical deflection at midspan in Figure 25 have been calculated using the measured values of b, h and h_c as shown in Table 2, the values of $E_{c,f}$ and $\varepsilon_{c,el}$ obtained using the midspan strain method as shown in Table 3, E_{fg} = 7589 N/mm^2 and a value of $\sigma_{c,c}$ = 2.11 N/mm^2 based on compression test results [14] summarised in Table 5. Since $E_{c,f}$ has been determined according to a strain-based method that

utilises the experimental values of M, the close agreement observed across the initial linear elastic regime of the moment–deflection curves is somewhat to be expected. The close agreement observed across the plastic regime, in particular for specimens P25, P26 and P28 shown in Figure 25a, b and d, respectively, depends on the accurate estimation of $\varepsilon_{c,el}$ and $\sigma_{c,c}$ and the validity of the stress–strain relationship shown in Figure 23, and thus serves to validate its use when deriving Eq.(9). In the case of specimen P27 shown in Figure 25c, it can be seen that the model overestimates the flexural rigidity of the section in the plastic regime. This can be attributed to there being deterioration on the compression side of the specimen, which is also evidenced by the compression-side delamination failure shown in Figure 20a, causing the method to over-predict the elastic range of the bead core material in compression. In the case of specimen P27, the accuracy of the prediction of Eq.(9) could be improved by defining a compressive failure strain but it would be superfluous for the vast majority of specimens where the failure mechanism initiates on the tension side.

3.2 Ultimate moment resistance

Having shown that the strain-based model described by Eq.(9) can provide accurate predictions for the bending moment, it is now adapted to calculate the ultimate moment resistance. Strain-based methods for determining the design resistance of structural elements have gained currency in recent years, with the continuous strength method [40] for the design of steel [41], stainless steel [42] and aluminium [43] members being a prominent example. In the case of these ductile metallic materials, the use of a strain-based method is advantageous by taking account of the considerable deformation capacity available before fracture. In the context of RGBSPs, the benefit of the strain-based method arises from exploiting the considerable elastic stiffness of the fibreglass facing sheets that serve to reinforce the more brittle bead core so that it can accommodate strains in excess of the limiting elastic strain. Although the contribution of the core is sometimes ignored when calculating the moment resistance of sandwich panels in order to simply calculations [6,12], neglecting to include the contribution of the bead core in the context of the present study would be overly conservative. In Figure 26, using specimen P28 as a representative example, the relative moment contributions of the fibreglass sheets, the portion of the bead core undergoing elastic deformation and the portion of the bead core undergoing plastic deformation, as calculated by Eq.(9), are plotted against the maximum tensile strain in the bead core $\varepsilon_{c,t}$. It can be seen that, initially, the elastic resistance of the bead core is in fact the predominant contributor to the overall moment resistance. After softening initiates on the tension side, the plastic resistance of the bead core is activated and the overall flexural rigidity of the bead core decreases, with the relative contribution of the fibreglass sheets increasing; however, even immediately prior to failure, the bead core still contributes approximately 25–30% of the moment resistance and thus greater economy is achieved by including the contribution of the bead core in design.

When considering the calculation of ultimate moments, Eq.(9) is simplified by neglecting the elastic contribution of the bead core, which is rational when considering the relative moment contributions shown in Figure 26 at failure. Rectangular stress blocks are assumed to act across the fibreglass sheets, with the strains in the top and bottom fibreglass sheets assumed to be equal to the maximum compressive and tensile strains in the bead core, respectively. The predicted ultimate moment resistance M_R is thus given by Eq.(10):

$$M_{\mathrm{R}} = bh_{\mathrm{c}}t_{\mathrm{fg}}E_{\mathrm{fg}}\left(\frac{\varepsilon_{\mathrm{c,tf}}^2 + \varepsilon_{\mathrm{c,cf}}^2}{\varepsilon_{\mathrm{c,tf}} + \varepsilon_{\mathrm{c,cf}}}\right) + \frac{1}{2}bh_{\mathrm{c}}^2E_{\mathrm{c,f}}\left(\varepsilon_{\mathrm{c,el}}\left(\frac{\varepsilon_{\mathrm{c,tf}}}{\varepsilon_{\mathrm{c,tf}} + \varepsilon_{\mathrm{c,cf}}}\right)^2\left(1 - \left(\frac{\varepsilon_{\mathrm{c,el}}}{\varepsilon_{\mathrm{c,tf}}}\right)^2\right) + \frac{\sigma_{\mathrm{c,c}}}{E_{\mathrm{c,f}}}\left(\frac{\varepsilon_{\mathrm{c,cf}}}{\varepsilon_{\mathrm{c,tf}} + \varepsilon_{\mathrm{c,cf}}}\right)^2\left(1 - \left(\frac{\sigma_{\mathrm{c,c}}}{\varepsilon_{\mathrm{c,cf}}E_{\mathrm{c,f}}}\right)^2\right)\right)$$

(10)

where $\varepsilon_{\mathrm{c,cf}}$ and $\varepsilon_{\mathrm{c,tf}}$ are the maximum compressive and tensile strains in the bead core at failure, respectively. Values of M_{R} / b that have been calculated using the measured geometric dimensions, the values of $E_{\mathrm{c,f}}$ and $\varepsilon_{\mathrm{c,el}}$ obtained using the midspan deflection method, E_{fg} = 7589 N/mm^2 and the average values of $\sigma_{\mathrm{c,c}}$ obtained from compressive testing, are shown in Table 6 for all the specimens tested in the present study and previously [14]. Based on the strains at failure shown in Figures 7 and 21, the values of $\varepsilon_{\mathrm{c,cf}}$ and $\varepsilon_{\mathrm{c,tf}}$ are assumed conservatively to be 0.35% and 0.50%, respectively, for the 1–2 mm bead cores and 0.45% and 0.60%, respectively, for the 4–8 mm bead cores. Given that the bead core is assumed to behave in an elastic–perfectly plastic manner, it is the definition of these strains at failure that govern the ultimate resistance of the RGBSPs and inform the strain-based nature of the resistance model.

In Figure 27, values of the experimental ultimate moment per metre width M_{u} / b are plotted against the values of M_{R} / b. It can be seen that, overall, Eq.(10) provides safe-sided predications for the ultimate moment while not being overly conservative and is thus suitable for use as the basis of a design method for determining the moment resistance of recycled glass bead sandwich panels in bending. The average values of $M_{\mathrm{u}} / M_{\mathrm{R}}$ are 1.24 for the 1–2 mm bead cores and 1.18 for 4–8 mm bead cores. In panels where the actual tensile failure strain is noticeably greater than the assumed value of $\varepsilon_{\mathrm{c,tf}}$, the elastic moment contribution of the bead core is more significant and thus neglecting it leads to more conservative predictions for the moment resistance. The specimens with increased polymer content and the previously-damaged specimens have all been shown to be somewhat more ductile than the other specimens and thus their moment resistances are more noticeably under-predicted when the assumed values of $\varepsilon_{\mathrm{c,cf}}$ and $\varepsilon_{\mathrm{c,tf}}$ are employed; if these specimens are discounted then the average value of $M_{\mathrm{u}} / M_{\mathrm{R}}$ for the 1–2 mm bead cores is 1.11.

3.3 Reliability analysis

While the development of a design standard for fibre-reinforced polymer structural elements is currently ongoing [44], structural elements containing particulate glass–polymer composites are not currently treated directly by structural design standards. According to EN 1990 [34], the principles of structural safety and reliability that form the basis of the European structural design framework can be extended to materials and structural systems that are not covered directly by its material-specific standards. Thus, a first-order reliability method (FORM) in accordance with Annex D of EN 1990 [34] is employed in the present study in order to assess the reliability of RGBSPs in bending and to calibrate a minimum required partial factor γ_{M} for use with the ultimate moment resistance function described by Eq.(10). Similar exercises have been conducted previously for hot-rolled steel sections [41], stainless steel sections [42,45], concrete-filled steel elliptical hollow section beam-columns [46], slender steel elliptical hollow sections [47], reinforced-concrete structures [48,49], FRP laminates [50] and FRP-strengthened reinforced-concrete structural

elements [51,52]; more detailed descriptions of the theoretical background to the methodology of these reliability analyses can be found in [45,48,53]. To the best of the author's knowledge, the reliability of structural elements containing particulate glass–polymer composites has not been assessed previously.

As stated in Cl.1.3(2) of EN 1990 [34], it is assumed that all materials used in the construction of a building structure shall meet the relevant product specifications upon delivery and that adequate supervision and quality control shall be provided during construction; in lieu of an existing standard concerning the technical delivery conditions of RGBSPs, compliance with internal quality control measures during manufacture, delivery and installation of the panels is thus assumed when assessing their reliability. In order to calibrate an appropriate partial factor of safety for RGBSPs that are suitable for use in construction, specimens P25 to P27, which had all experienced some form of damage prior to testing, have thus been discounted from the reliability analysis. In addition, the specimens with increased polymer content (P21 to P24) have also been discounted from the analysis since there is not enough data available to include the influence of polymer content in the resistance function with confidence – testing of specimens with a greater diversity of polymer volume fractions is recommended in order to inform such an analysis satisfactorily. Given that the strength of glass-polymer composites tends to increase with polymer content [30,31], it can be assumed that the design method provides conservative predictions for the moment resistance of RGBSPs with bead cores containing at least 7% polymer content by volume. In summary then, a total of 14 specimens containing 1–2 mm glass bead cores and 7 specimens containing 4–8 mm glass bead cores have been included in the present study.

The values of M_u / b form the set of experimental resistances $\mathbf{r_e}$ for the reliability analysis while the values of M_R / b form the set of theoretical resistances $\mathbf{r_t}$; the datasets are split into sub-groups based on the glass bead diameter range so that separate partial factors are determined for the 1–2 mm bead cores and 4–8 mm bead cores, respectively. According to Eq.(10), the moment resistance is a function of the set of basic variables $\underline{X} = \{E_{c,f}, \varepsilon_{c,el}, \sigma_{c,c}, \varepsilon_{c,cf}, \varepsilon_{c,tf}, b, h_c, t_{fg}\}$. The correlation between $\mathbf{r_e}$ and $\mathbf{r_t}$ is assessed using the slope of best fit b_r. In Annex D of EN 1990 [34] a least-squares function is recommended to determine b_r; however, this definition has been noted [45–47] to be biased towards specimens with higher resistances and thus in the present study the slope of best fit is given by:

$$b_r = \frac{1}{n}\sum \frac{r_{e,i}}{r_{t,i}} \tag{11}$$

where n is the number of specimens under consideration in a sub-group. In addition to the closeness of fit between the experimental and theoretical datasets, the calibration of the partial factor γ_M is also dependent on the variance of errors between the experimental and theoretical resistances V_δ and the variances of the basic variables V_{Xi}. Properties with larger variances necessitate higher partial factors in order to account for the increased uncertainties in the accuracy of the resistance function when using the characteristic values of the basic variables. The overall coefficient of variation of the resistance function V_r can be calculated as [34]:

$$V_r^2 = \left(1 + V_\delta^2\right)\left(\prod\left(1 + V_{X_i}^2\right)\right) - 1 \tag{12}$$

The average values, coefficients of variation and 5th percentile values of the material properties for the specimens under consideration are shown in Table 5; in particular, it can be seen that the variance in $\varepsilon_{c,el}$ for the 4–8 mm bead core material is relatively large. The coefficients of variation of the geometric properties b, h_c and t_{fg} are 0.004, 0.004 and 0.036, respectively. In the present study, the 5th percentile values are used as the characteristic values for the material properties,

whereas in accordance with EN 1990 [34] the nominal values of the geometric properties are taken as characteristic.

It is assumed that RGBSPs are intended for use in conventional residential, office and commercial building structures that fall under reliability class RC2 in the European structural design framework with a target reliability index $\beta = 3.8$ [34], which is equivalent to a probability of failure of 7.2×10^{-5} across the standard 50 year reference period. This level of reliability against ultimate failure is ensured in the analysis through the selection of an appropriate design fractile factor $k_{d,n}$ that reflects decreasing uncertainty with increasing sample size in accordance with Bayesian forecasting. As stated in Cl.D.8.2.2.5 of EN 1990 [34], although the dataset is split into two sub-groups, $k_{d,n}$ can be calculated on the basis of the total number of observations being considered, which is 21 in the present analysis. Adopting the standard evaluation procedure of section D8.3 of EN 1990 [34], the partial factor γ_M for the design method is defined as r_n / r_d. The nominal resistance r_n is conservatively based on the characteristic or nominal values of the basic variables, while the design resistance r_d is based on the mean values of the basic variables since the measured values have been used to calculate $\mathbf{r_t}$ originally; thus, the calculation of the partial factor involves the ratios of the mean values to the characteristic values. By conservatively taking the minimum ratios of mean to characteristic values of the material properties to be 1.12 for the 1–2 mm bead cores and 1.15 for the 4–8 mm bead cores, the minimum required partial factors γ_M are found to be 1.40 and 2.20, respectively; the results of the reliability analysis and the parameters employed therein are shown in Table 7. Considering the 1–2 mm bead cores, it is noted that the value of 1.40 for the partial factor is similar to the material partial factor for concrete $\gamma_C = 1.50$ in the European structural design framework [37], although the characteristic strength of concrete is based on average values rather than 5th percentiles. Thus, employing $\gamma_M = 1.40$ can be considered appropriate for determining the design moment resistance of recycled glass bead sandwich panels containing 1–2 mm bead cores with a minimum of 7% polymer content by volume. Since the required partial factor for the 4–8 mm bead cores is more onerous, it is recommended that panels containing such cores be used in scenarios where load resistance is not the primary criteria for functionality, e.g., single-storey or temporary structures. Although including additional experimental results and the results of numerical analyses, as has been done previously [46–50], in the dataset would lower the required design fractile factor and might reduce the variance of the errors, the measured variances in the material properties must also decrease substantially for there to be a significant reduction in the required partial factor. In the absence of other published literature, the present analysis assumes conservatively that the variances in material properties shown in Table 5 are representative of the population. It is also possible that including a set of numerical results that underestimate the experimental resistances significantly would in fact lead to an overestimation of the minimum required value of γ_M since the discrepancy between the average experimental result and the average numerical result would lead to an artificial increase to the variance of the errors V_δ. In any case, since the mode of failure of the bead core is brittle, it is prudent to employ a conservative value of γ_M in order to ensure additional safety and reliability in the design and application of RGBSPs in practice. The design moment resistance M_{Rd} is calculated by applying γ_M to M_R calculated using the characteristic values of the basic variables $\underline{X}_k$ thus:

$$M_{Rd} = \frac{M_R\{\underline{X}_k\}}{\gamma_M} \tag{13}$$

A conservative value of E_{fg} = 7500 N/mm^2 has also been assumed; a characteristic value of 8000 N/mm^2 is quoted in technical guidance [39]. In Figure 28, values of the ratio of the experimental ultimate moment to the design moment resistance M_u / M_{Rd} are plotted against values of δ_u / L for all undamaged specimens including the flexural specimens. It can be seen that the design predictions

are conclusively safe-sided when compared to the experimental results across the range of glass bead diameters, panel depths and polymer volume fractions considered in the present study.

4. Conclusions

An investigation has been conducted into the structural behaviour of sandwich panels comprising a core of recycled glass beads bound in polymer resin enveloped by fibreglass facing sheets. Flexural testing of small-scale beam specimens has been conducted whereby samples cut from full panels are loaded in four-point bending. A method of determining the elastic properties of the bead core material based on the maximum tensile and compressive strains at midspan has been found to provide values of the elastic flexural modulus, the limiting elastic strain and the limiting elastic strength of the bead core material that are broadly in line with previous results that were derived through the analysis of vertical deflections at midspan.

Four-point bending tests have been conducted on a range of full-scale panel specimens of varying spans, bead core contents and adhesive strengths. While it was found that the use of a high-strength adhesive between the bead core and the fibreglass facing sheets is not accompanied by any appreciable improvement in structural performance, the inclusion of additional polymer content leads to noticeable increases in the ultimate resistance and deformation capacity of the panels. Experiments conducted on specimens cut from panels that had been tested previously have shown the potential benefits of preloading panels in compression so that the overall deformation capacity of a panel in bending is enhanced.

Values of the flexural modulus determined through analysis of midspan strains are found to be approximately 20% greater than those found using the midspan deflection method. In order to encourage additional safety in design, it is recommended that values of the flexural modulus can be based on values found by using the midspan deflection method for specimens where $L / h > 8$. If the flexural modulus is to be determined for more stocky specimens, the midspan strain method is recommended.

Midspan bending strain distributions are used to inform a model for predicting the applied bending moment; close agreement is observed between the experimental and predicted moment–deflection curves. When adapted to predict ultimate moments, the model is found to provide safe-sided predictions compared to the experimental results. The results of a reliability analysis of the predicted ultimate resistances of recycled glass bead sandwich panels in bending suggest that a partial factor of 1.40 is safe for use when determining the bending resistance of panels containing 1–2 mm bead cores with a polymer content of at least 7% by volume. A partial factor of 2.20 is recommended for 4–8 mm bead cores; given the reduced economy in design associated with such a large factor of safety, it is recommended that panels containing 4–8 mm bead cores be used in light-loading scenarios where structural resistance is not the primary selection criteria in terms of functionality. A comparison of the design ultimate moments incorporating the recommended partial factors against the experimental results has shown that the design moment resistances are conclusively safe-sided across a range of glass bead diameters, panel depths and bead core contents.

6. Acknowledgements

This research is supported by the School of the Built Environment and Architecture and the CCiBSE research centre at London South Bank University. All experimental specimens were supplied by Vitromite Ltd. The author wishes to extend his gratitude to Mr Paul Elsdon and Mr Graham Bird of the Strengths of Materials laboratory at London South Bank University for their expertise and dedication in conducting the experiments, while special thanks is also expressed to students Mr

Abid Ahmadzai, Mr Mekuria Kassaye, Mr Ahmad Seedat and Miss Aimee Smith for their invaluable assistance in conducting the experiments.

7. Data availability statement

The raw and processed data required to reproduce these findings are available to download from https://www.researchgate.net/publication/344351547_RGBSP_test_data.

References

1. R. Jin, S. Gao, A. Cheshmehzangi, E. Aboagye-Nimod. 2018. A holistic review of off-site construction literature published between 2008 and 2018, *Journal of Cleaner Production*, 202:1202–1219.
2. Z. Li, G.Q. Shen, X. Xue. 2014. Critical review of the research on the management of prefabricated construction. *Habitat International*, 43:240–249.
3. D. Zenkert. 1995. An introduction to sandwich construction. London: Engineering Materials Advisory Services Ltd.
4. M.F. Ashby, Y.J.M. Bréchet. 2003. Designing hybrid materials. *Acta Materialia*, 51:5801–21.
5. S Yiatros. 2010. Mode interaction and localization in sandwich struts and beam-columns. PhD thesis. Imperial College London, April 2010.
6. N.A. Fleck, I. Sridhar. 2002. End compression of sandwich columns. *Composites Part A: Applied Science & Manufacturing.*, 33:353–359.
7. R. O′ Hegarty, R. West, A. Reilly, O. Kinnane. 2018. Composite behaviour of fibre-reinforced concrete sandwich panels with FRP shear connectors, *Engineering Structures*, 198:109475.
8. S. Darzi, H. Karampour, H. Bailleres, B.P. Gilbert, R.L. McGavin. 2020. Experimental study on bending and shear behaviours of composite timber sandwich panels, *Construction & Building Materials*, 259:119723.
9. M. Kulpa, T. Siwowski. 2019. Stiffness and strength evaluation of a novel FRP sandwich panel for bridge redecking. *Composites Part B: Engineering*, 167:207–220.
10. L. Santos, A.N. Nordas, B.A. Izzudin, L. Macorini. 2018. Structural design optimisation of rectangular honeycomb core sandwich panels under out-of-plane loading", 12th International Conference on Sandwich Structures, 19–22 August 2018, Lausanne, Switzerland.
11. V.S. Deshpande, N.A. Fleck. 2000. Isotropic constitutive models for metallic foams, *Journal of the Mechanics and Physics of Solids*, 48:1253–1283.
12. B.H. Smith, S. Szyniszewski, J.F. Hajjar, B.W. Schafer, S.R. Arwade. 2012. Steel foam for structures: A review of applications, manufacturing and material properties, *Journal of Constructional Steel Research*, 71:1–10.
13. R. Stewart. 2011. 'Composites in construction advance in new directions', *Materials Today*, 6 September 2011.
14. H. Aygün, F. McCann. 2020. Structural and acoustical performance of recycled glass bead panels. *Construction and Building Materials*, 258:1–13.
15. A. Zaman, S.A. Gutub, M.A. Wafa. 2013. A review on FRP composites applications and durability concerns in the construction sector, *Journal of Reinforced Plastic and Composites*, 32(24):1966–1988.

16. T. S. Serniabat, M. N. N. Khan, M. F. M. Zain. 2014. Use of Waste Glass as Coarse Aggregate in Concrete: A Possibility towards Sustainable Building Construction, *International Journal of Civil and Environmental Engineering* 8(10), 2014.
17. A. Mohajerani, J. Vajna, T. Ho, H. Cheung, H. Kurmus, A. Arulrajah, S. Horpibulsuk. 2017. Practical recycling applications of crushed waste glass in construction materials: A review, *Construction and Building Materials*, 156:443–467,
18. J. Tao. 2017. Use of Crushed Recycled Glass in the Construction of Local Roadways. Ohio's Research Initiative for Locals, The Ohio Department of Transportation Office of Statewide Planning and Research, Technical Report 135329.
19. Z.T. Abu Salem, T.S. Khedawi, M.B. Baker, R. Abendeh. 2017. Effect of waste glass on properties of asphalt concrete mixtures, *Jordan Journal of Civil Engineering*, 11(1):117–131.
20. I. Demir. 2009. Reuse of waste glass in brick production. *Waste Management & Research*, 27:572–577.
21. C. Jofeh. 2016. 'Strength and durability of glass', in M. Forde (ed.), *ICE Manual of Construction Materials*, London: Institution of Civil Engineers, 807–812.
22. A-H.I. Mourad, A.H. Idrisi, M.C. Wrage, B.M. Abdel-Magid. 2019. Long-term durability of thermoset composites in seawater environments, *Composites Part B*, 168:243–253.
23. M. Tascan, K. Lyon Gaffney. 2012. Effect of glass-beads on sound insulation properties of nonwoven fabrics, *Journal of Engineered Fibres and Fabrics*, 7(1):101–105.
24. M.F. Ashby. 1983. Mechanical properties of cellular solids. *Metallurgical Transactions A*, 14A(9):1755–1769.
25. E.E. Gdoutos, I.M. Daniel, K. A. Wang. 2003. Compression facing wrinkling of composite sandwich structures, *Mechanics of Materials*, 35:511–522.
26. C.A. Steeves, N.A. Fleck. 2004. Collapse mechanisms of sandwich beams with composite faces and a foam core, loaded in three-point bending. Part I: analytical models and minimum weight design. *International Journal of Mechanical Sciences*, 46:561–583.
27. G.W. Hunt, M.A. Wadee. 1998. Localization and mode interaction in sandwich structures. *Proceedings of the Royal Society* A, 454:1197–1216.
28. M.A. Wadee, A. Blackmore. 2001. Delamination from localized instabilities in compression sandwich panels. *Journal of the Mechanics and Physics of Solids*, 49(6):1281–1299.
29. Y. Frostig. 1992. Behavior of delaminated sandwich beam with transversely flexible core – high-order theory. *Composite Structures*, 20(1):1–16.
30. S.-Y. Fu, X.-Q. Feng, B. Lauke, Y.-W. Mai. 2008. Effects of particle size, particle/matrix interface adhesion and particle loading on mechanical properties of particulate–polymer composites, *Composites: Part B*, 39:933–961.
31. R.J. Young, P.W.R. Beaumount. 1977. Effect of composition upon fracture of silica particle-filled epoxy–resin composites. *J. Mater. Sci.*, 12:684-692.
32. D.A. Vajari, B.F. Sørensen, B.N. Legarth. 2015. Effect of fiber positioning on mixed-mode fracture of interfacial debonding in composites, *International Journal of Solids and Structures*, 53:58–69.
33. J. Guilleminot, D. Kondo, C. Binetruy, S. Panier, S. Hariri, P. Krawczak. 2007. A micromechanical analysis of a local failure criterion for particle-reinforced composites, *Composite Science and Technology*, 67:2384–2389.
34. Comité Européen de Normalisation. 2002. *EN 1990:2002 Eurocode – Basis of structural design*, CEN, 2002.
35. S. Zhang, X. Gao, J. Chen, H. Dong, Y. Song, H. Zhang. 2016. Effect of micro-damage on the nonlinear constitutive behavior of SiC/SiC minicomposites. *Journal of Ceramic Science & Technology*, 7:341–348.

36. Y. Wang, L. Cheng, L. Zhang. 2017. Prediction of the mechanical behavior of a minicomposite based on grey Verhulst models. *Ceramics-Silikaty*, 61:372–377.
37. Comité Européen de Normalisation. 2004. EN 1992-1-1:2004 Eurocode 2. Design of Concrete Structures—Part 1: General Rules and Rules for Buildings, CEN, 2004.
38. ACI Committee 318. 1995. Building Code Requirements for Reinforced Concrete (ACI 318RM-95) and Commentary (ACI 318RM-95). Mich.: American Concrete Institute, Farmington Hills.
39. Performance Composites Inc. 2015. "Fiberglass and Composite Material Design Guide" (technical guide). Performance Composites Inc: Compton, USA. 2015.
40. L. Gardner. 2008. The Continuous Strength Method. *Proceedings of the Institution of Civil Engineers - Structures and Buildings*. 161(3):127–133.
41. X. Yun, L. Gardner, N. Boissonade. 2018. The continuous strength method for the design of hot-rolled steel cross-sections. *Engineering Structures*, 157:179–191.
42. S. Afshan, L. Gardner. 2013. The continuous strength method for structural stainless steel design. *Thin-Walled Structures*, 68:42–49.
43. M.N. Su, B. Young, L. Gardner. 2013. Continuous Strength Method for Aluminium Alloy Structures. *Advanced Materials Research*, 742:70–75
44. L. Ascione, J.-F. Caron, P. Godonou, K. van IJselmuijden, J. Knippers, T. Mottram, M. Oppe, M. Gantriis Sorensen, J. Taby, L. Tromp. 2016. Prospect for new guidance in the design of FRP; EUR 27666 EN.
45. S. Afshan, P. Francis, N.R. Baddoo, L. Gardner. 2015. Reliability analysis of structural stainless steel design provisions. *Journal of Constructional Steel Research*, 114:293–304.
46. W. Qiu, F. McCann, A. Espinos, M.L. Romero, L. Gardner. 2017. Numerical analysis and design of slender concrete-filled elliptical hollow section columns and beam-columns, *Engineering Structures*, 131:90–100.
47. F. McCann, L. Gardner. 2019. Numerical analysis and design of slender elliptical hollow sections in bending. *Thin-Walled Structures*, 139:196–208.
48. D. Seo, S. Shin, B. Han. 2010. Reliability-based structural safety evaluation of reinforced concrete members. *Journal of Asian Architecture and Building Engineering*, 9(2):471–478.
49. E.G. Abdelouafi, K. Benaissa, K. Abdellatif. 2015. Reliability analysis of reinforced concrete buildings: comparison between FORM and ISM. *Procedia Engineering*, 114:650–657.
50. S.L. Omairey, P.D. Dunning, S. Sriramula. 2019. Multiscale surrogate-based framework for reliability analysis of unidirectional FRP composites, *Composites Part B*, 173:106925.
51. S.E.C. Ribeiro, S.M.C. Diniz. 2013. Reliability-based design recommendations for FRP-reinforced concrete beams, *Engineering Structures*, 52:273–283.
52. X. Huang, Y. Zhou, F. Xing, Y. Wei, L. Sui, N. Han. 2020. Reliability-based design of FRP flexural strengthened reinforced concrete beams: Guidelines assessment and calibration, *Engineering Structures*, 209:109953.
53. T. Tankova, L. Simoes da Silva, L. Marques, C. Rebelo, A. Taras. 2014. Towards a standardized procedure for the safety assessment of stability design rules. *Journal of Constructional Steel Research*, 103:290–302.

a) b)

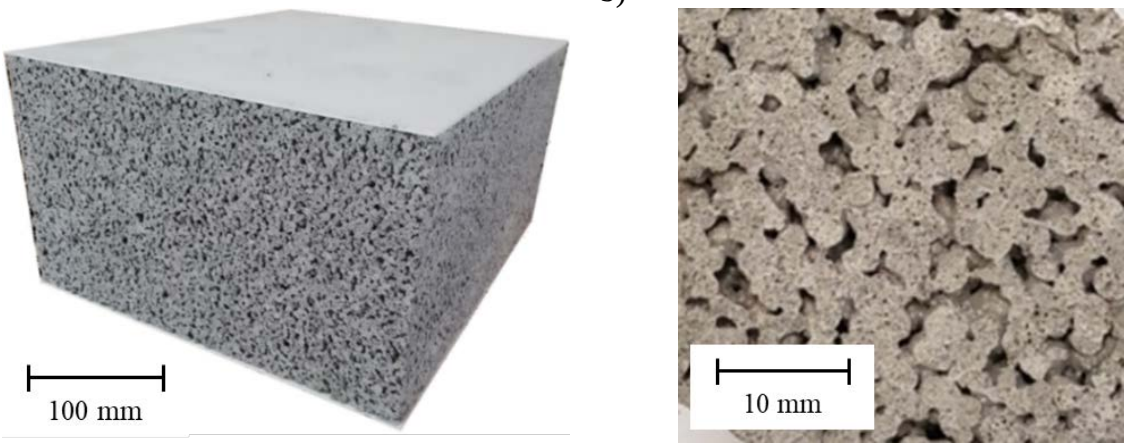

Figure 1: a) Sample of recycled glass bead sandwich panel; b) detail of recycled glass bead core showing entrapped voids.

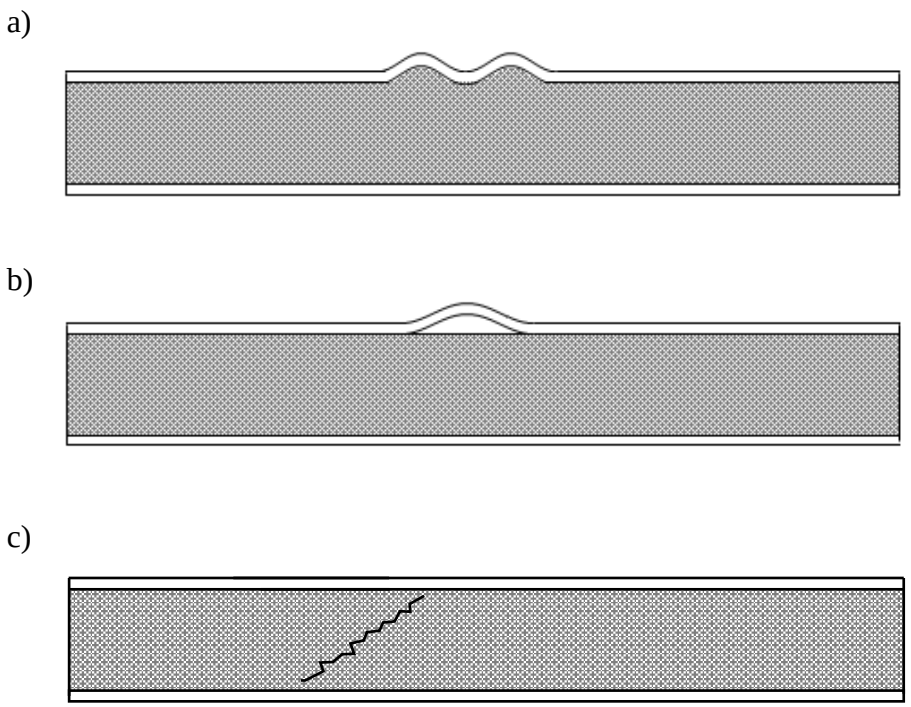

Figure 2: Examples of typical failure modes in sandwich panels in bending: a) facing sheet wrinkling; b) facing plate delamination; c) shear failure of core.

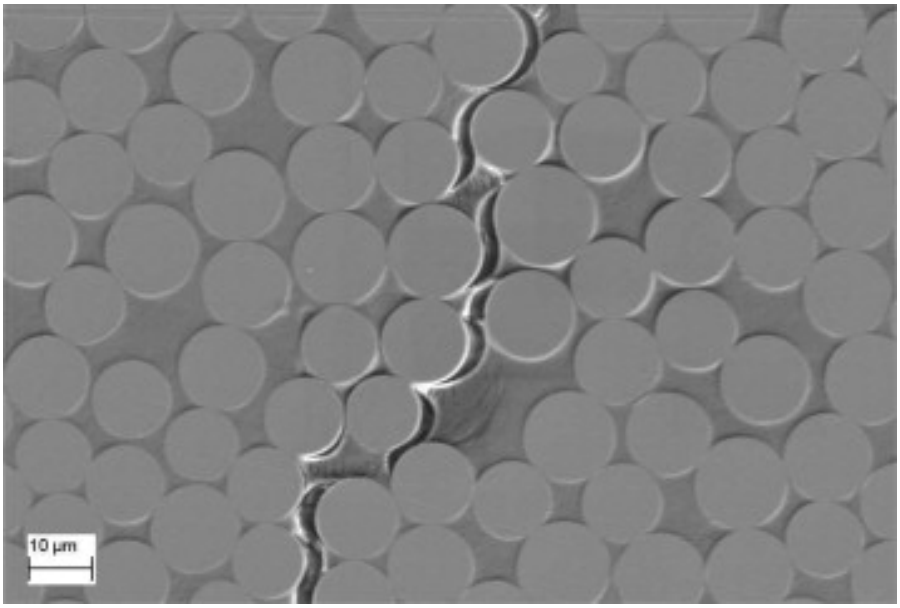

Figure 3: Example of interfacial debonding in a glass fibre–epoxy composite; reprinted from [32] with permission from Elsevier.

a)

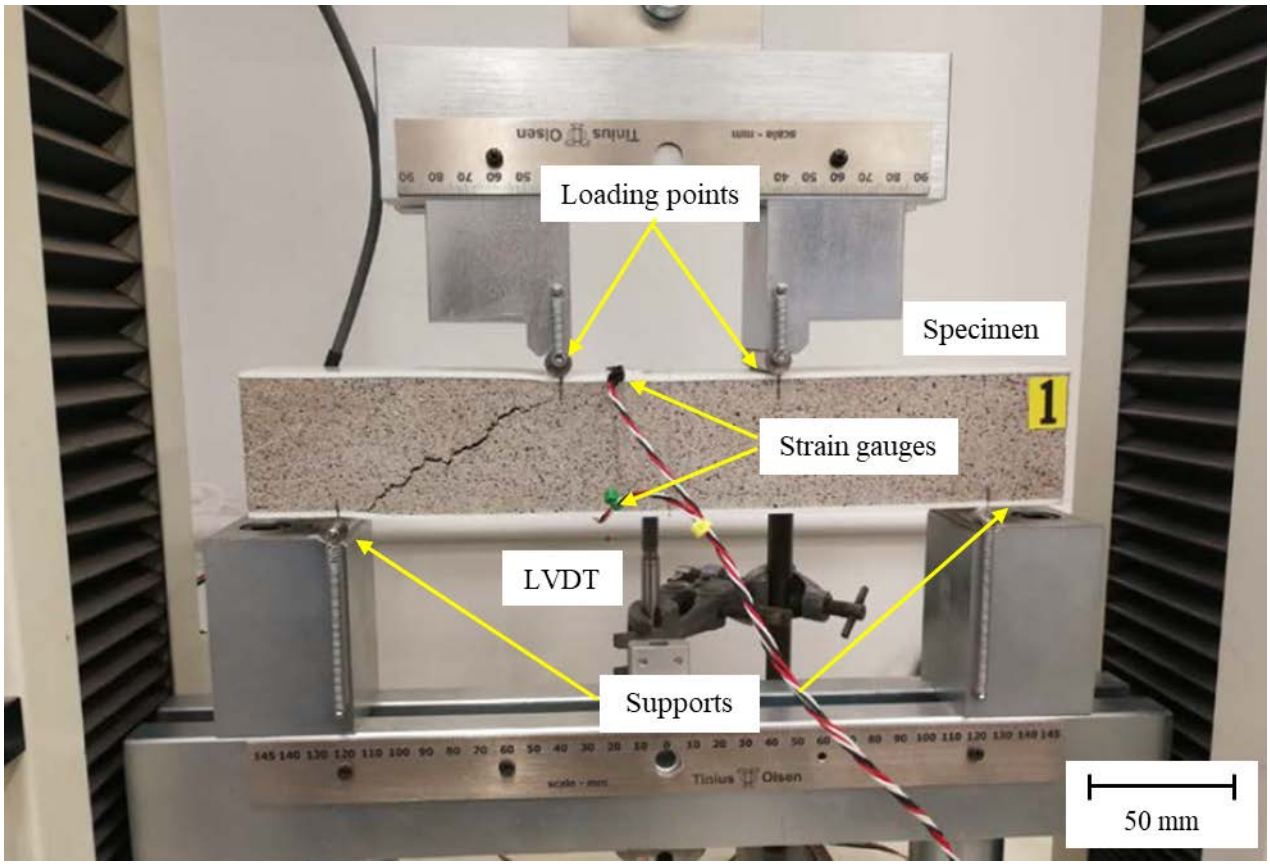

b)

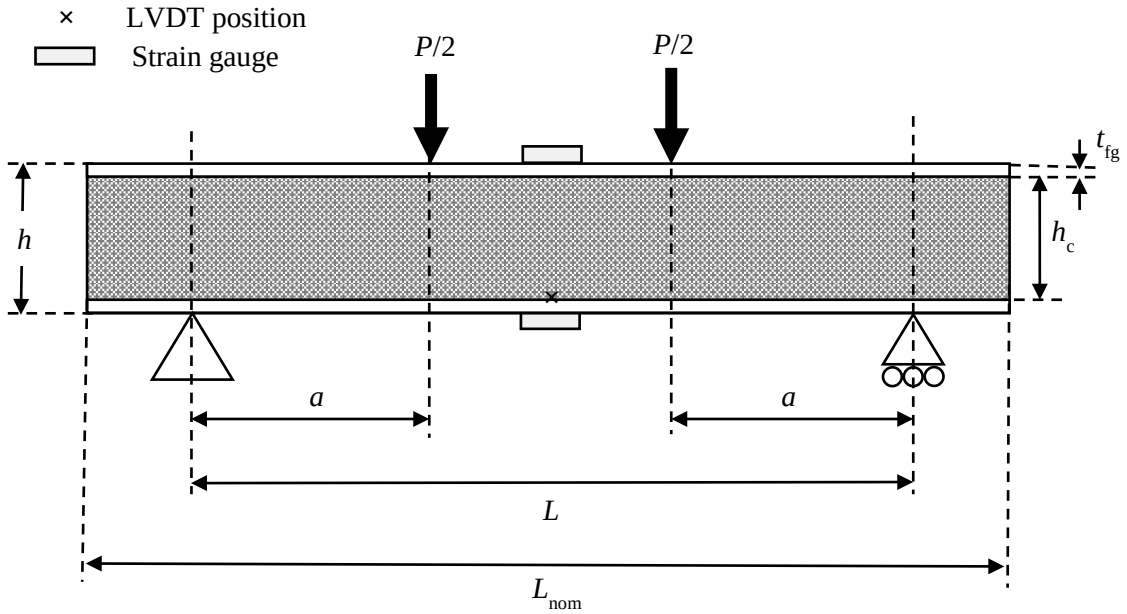

Figure 4: a) Specimen F01 after a four-point bending test in a Tinius Olsen HK25S universal testing machine; b) schematic of flexural and bending tests.

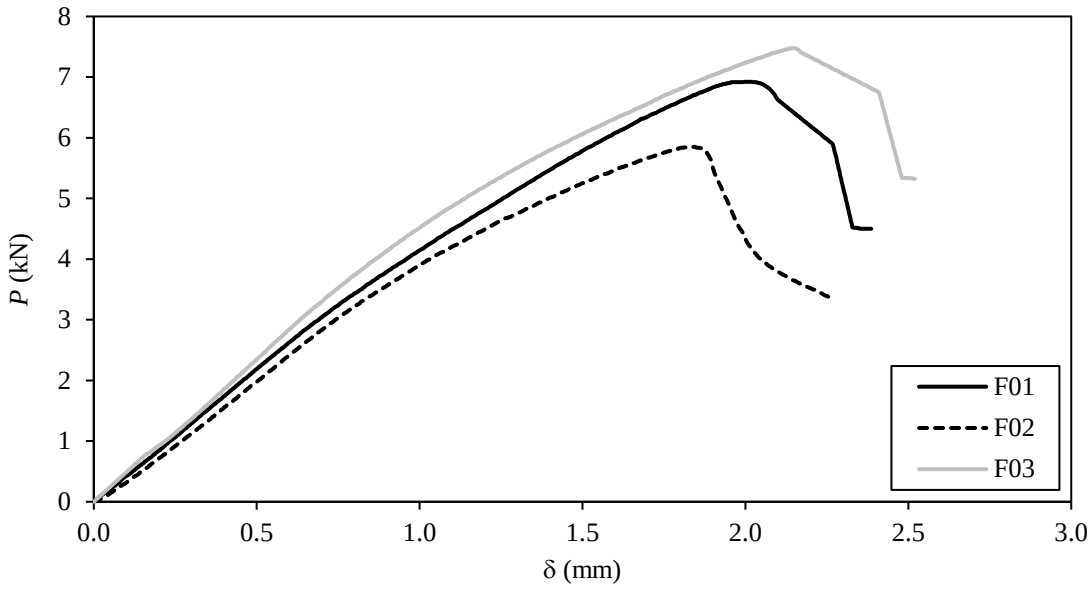

Figure 5: Load–deflection curves obtained from flexural testing.

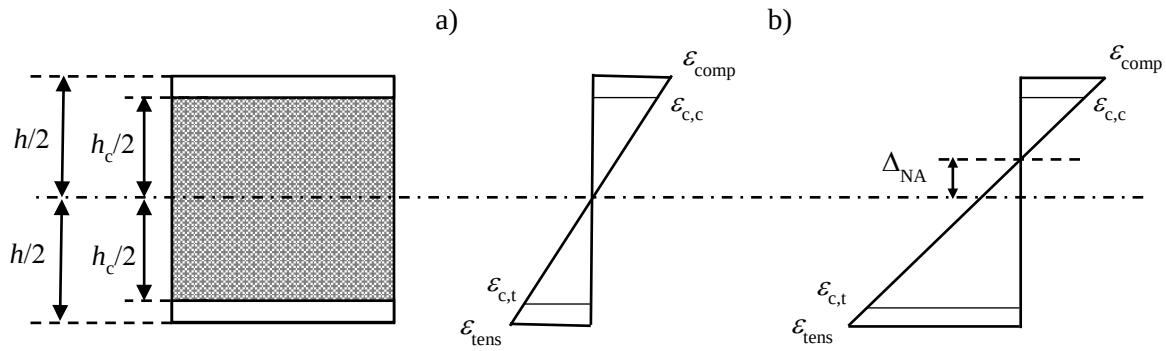

Figure 6: Longitudinal strain distributions assumed for a) $\varepsilon_{comp} / \varepsilon_{tens} = 1$; b) $\varepsilon_{comp} / \varepsilon_{tens} < 1$.

a)

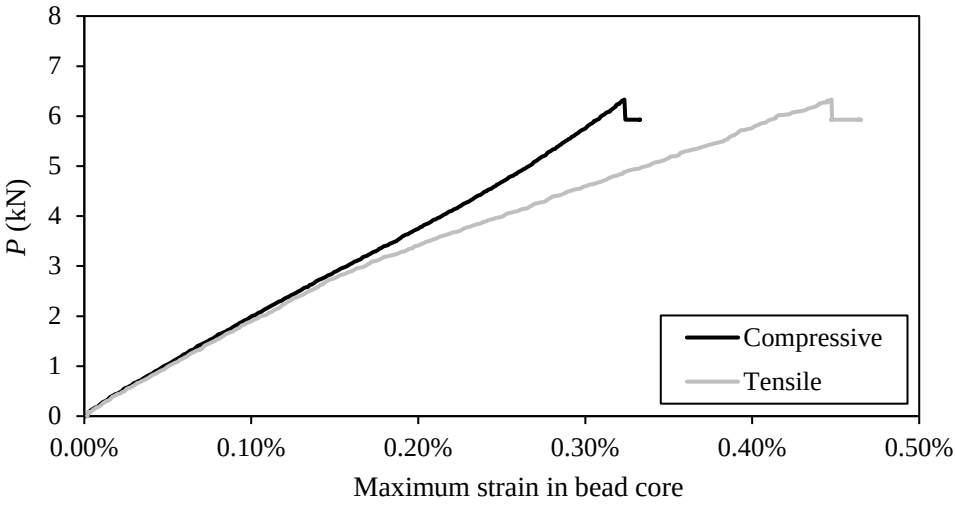

b)

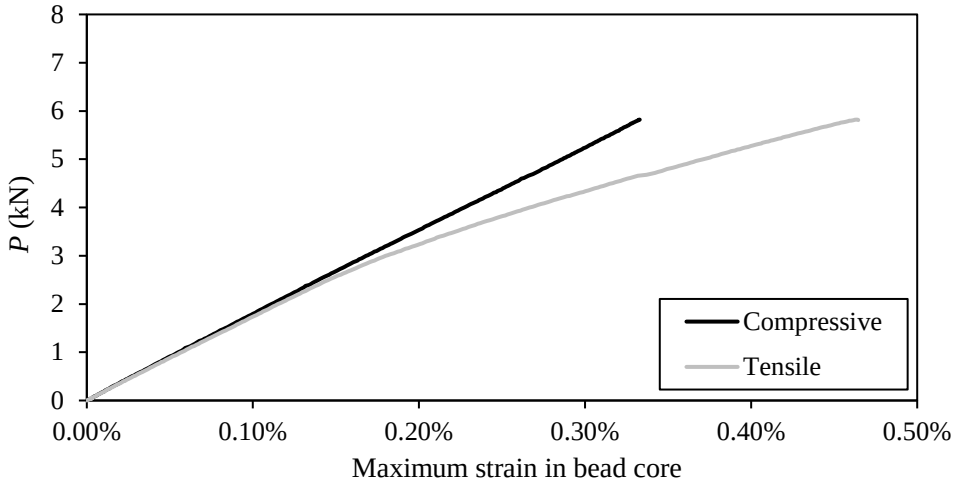

c)

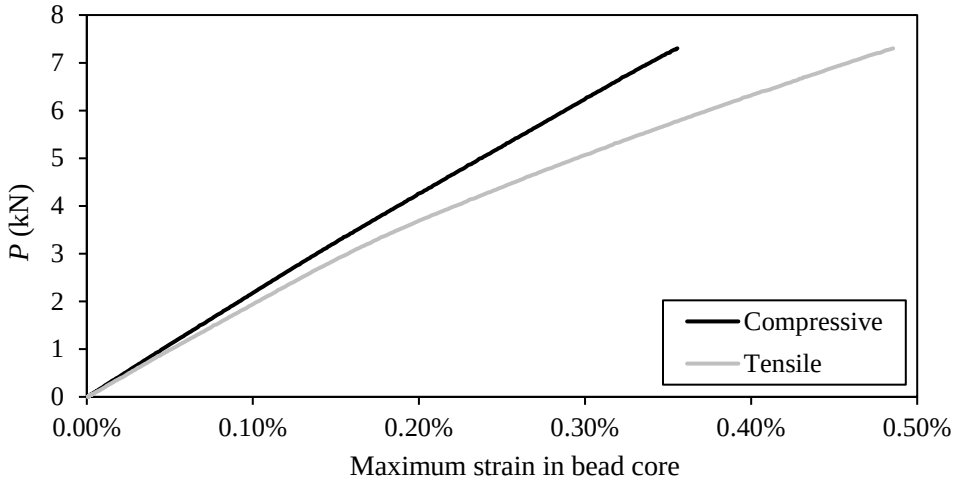

Figure 7: Maximum compressive and tensile strains in the bead core at midspan of a) specimen F01; b) specimen F02; c) specimen F03.

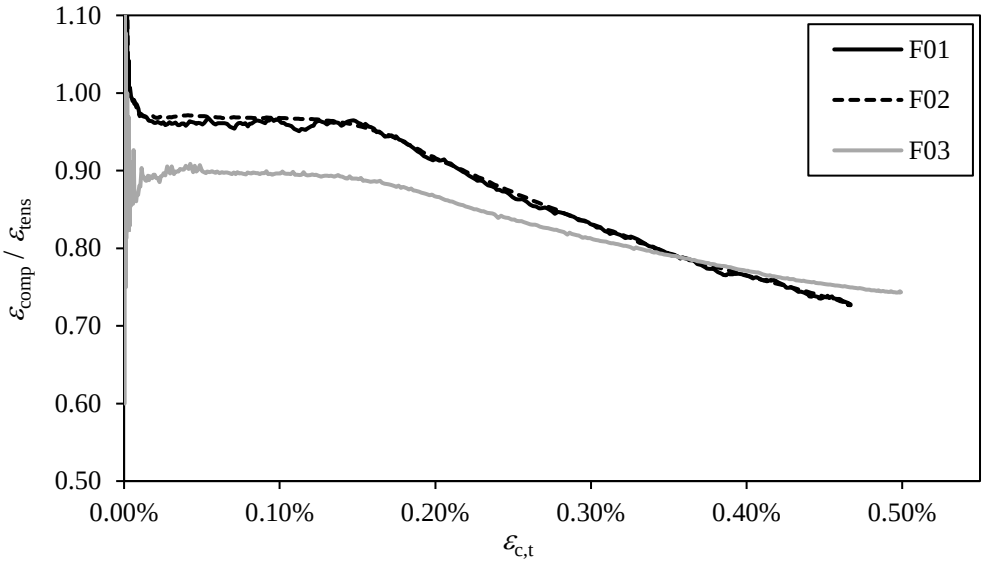

Figure 8: Ratio of compressive to tensile strains at extreme fibres during flexural tests.

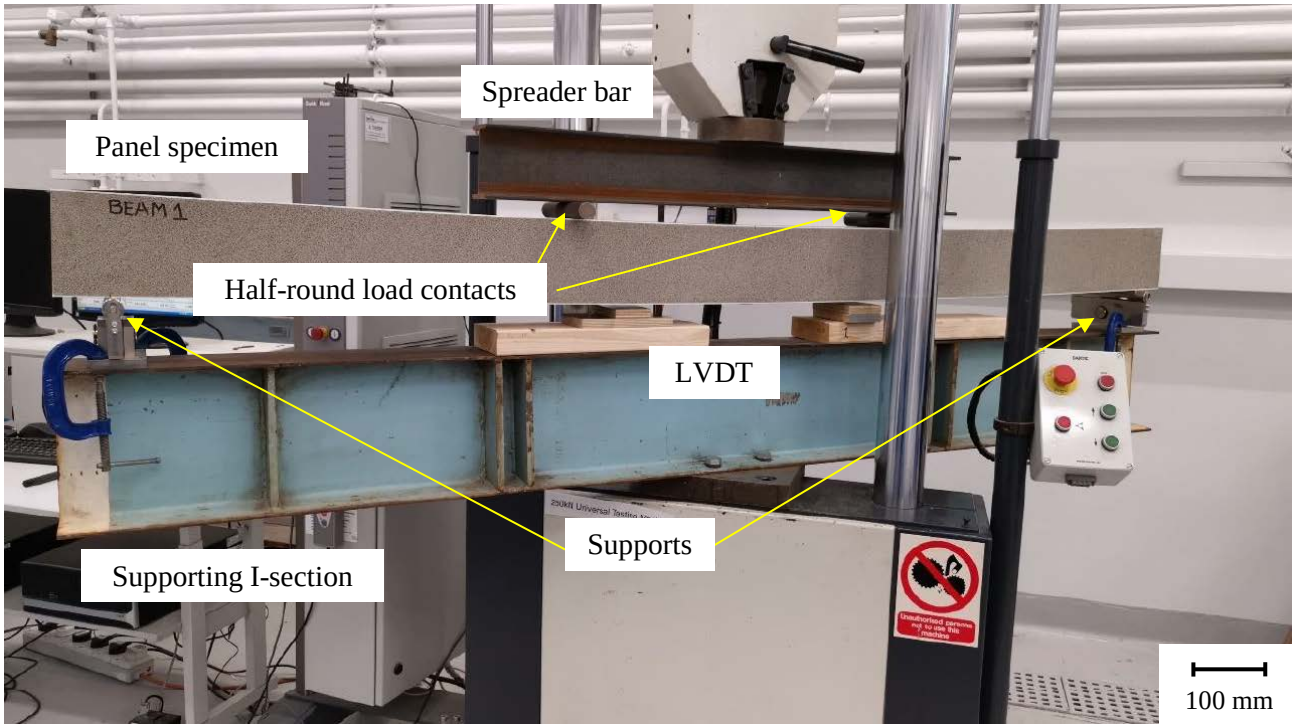

Figure 9: Four-point bending test set-up in Zwick/Roell 250 kN universal testing machine.

a)

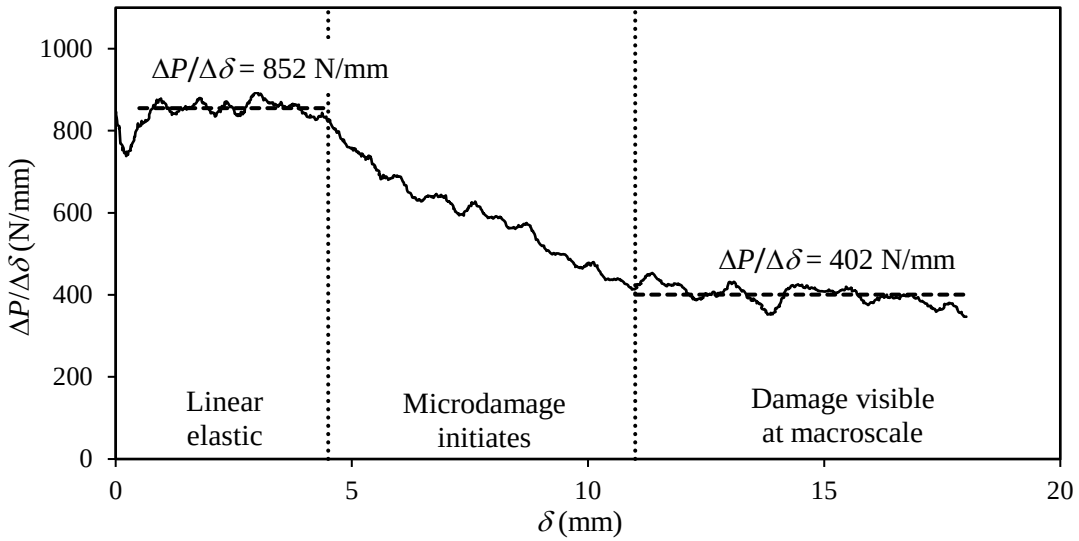

b)

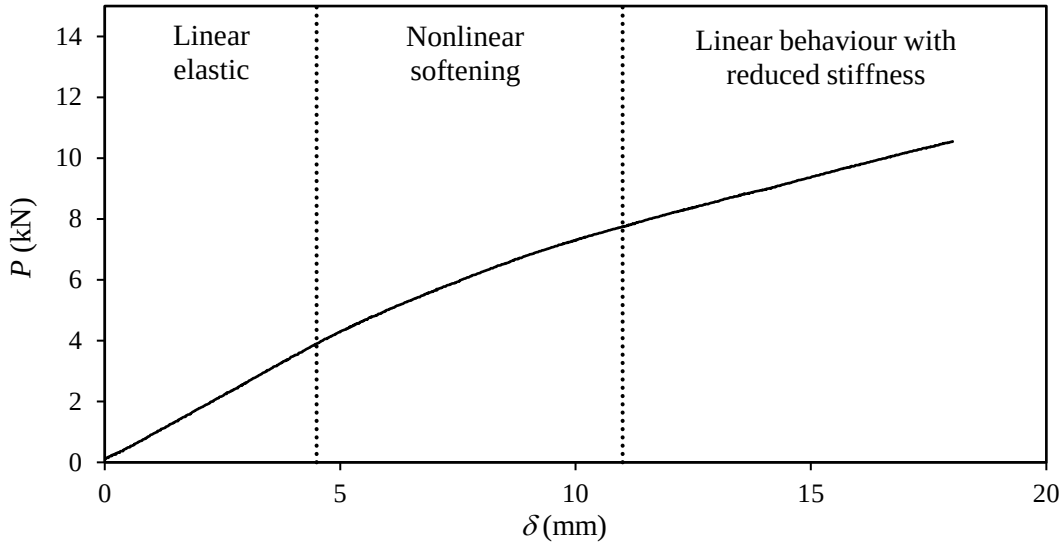

Figure 10: a) Typical graph of $\Delta P/\Delta\delta$ against midspan deflection δ (specimen P20 shown); b) corresponding graph of P against δ.

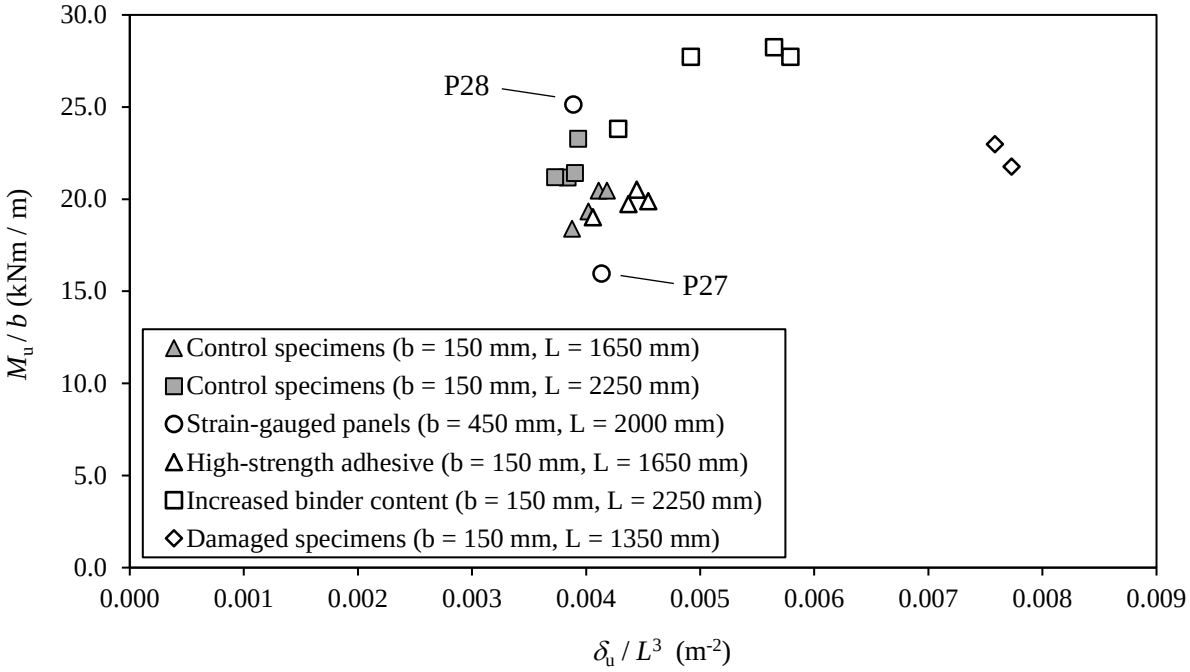

Figure 11: Values of M_u / b plotted against δ_u / L^3.

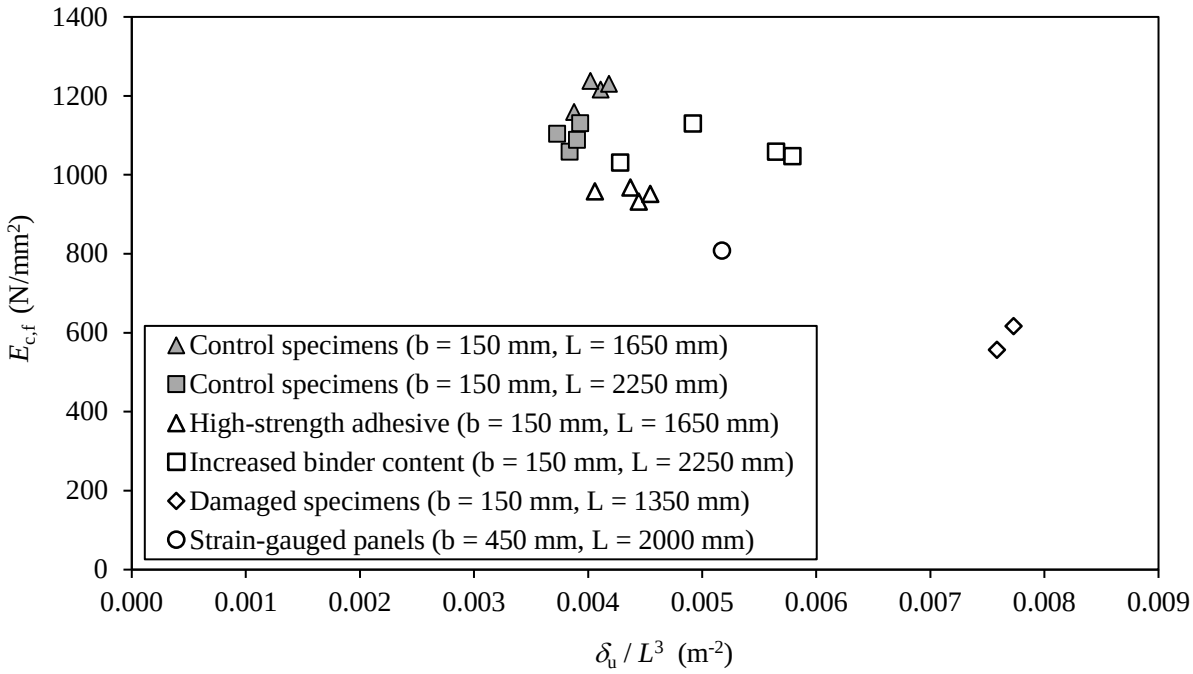

Figure 12: Values of $E_{c,f}$ plotted against δ_u / L^3.

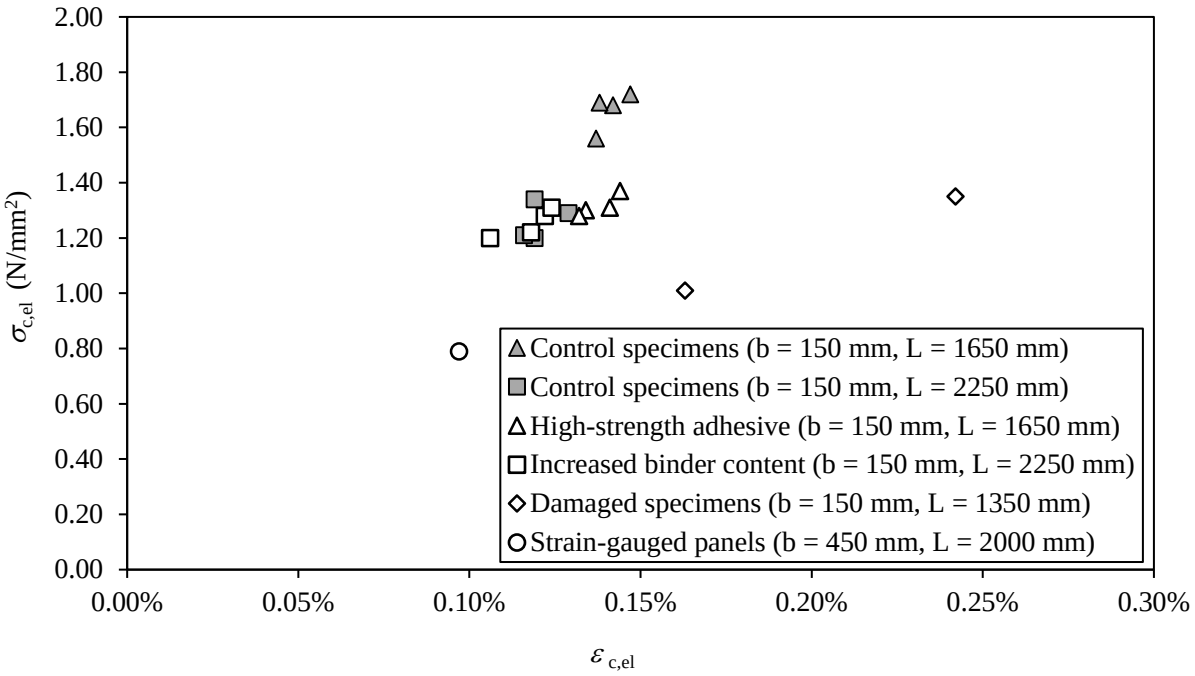

Figure 13: Values of $\sigma_{c,el}$ plotted against $\varepsilon_{c,el}$.

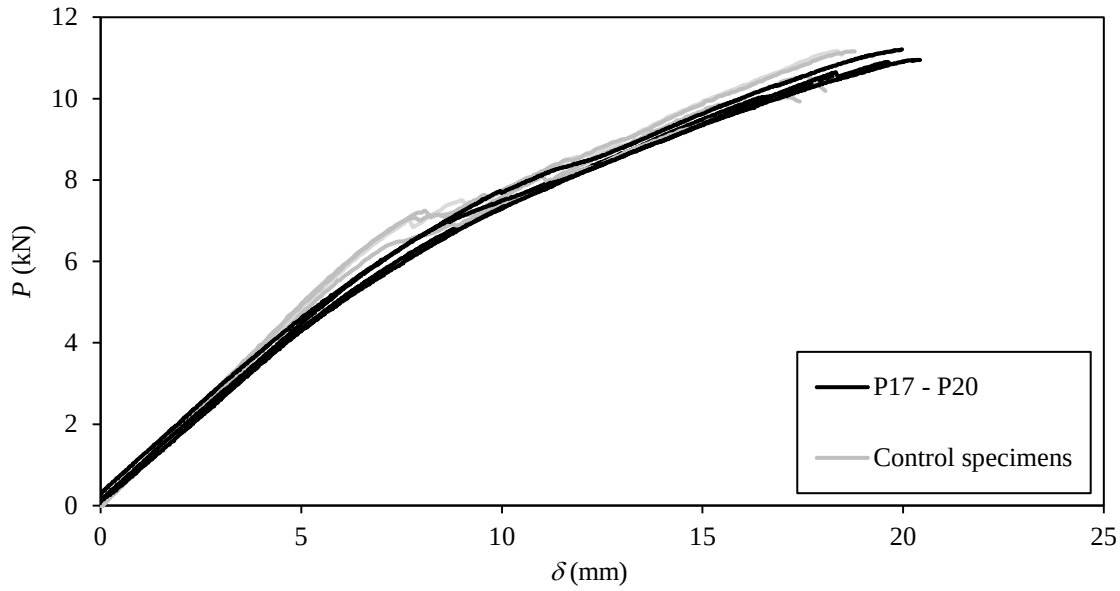

Figure 14: Load–deflection curves of specimens containing high-strength adhesive compared against those of the control group.

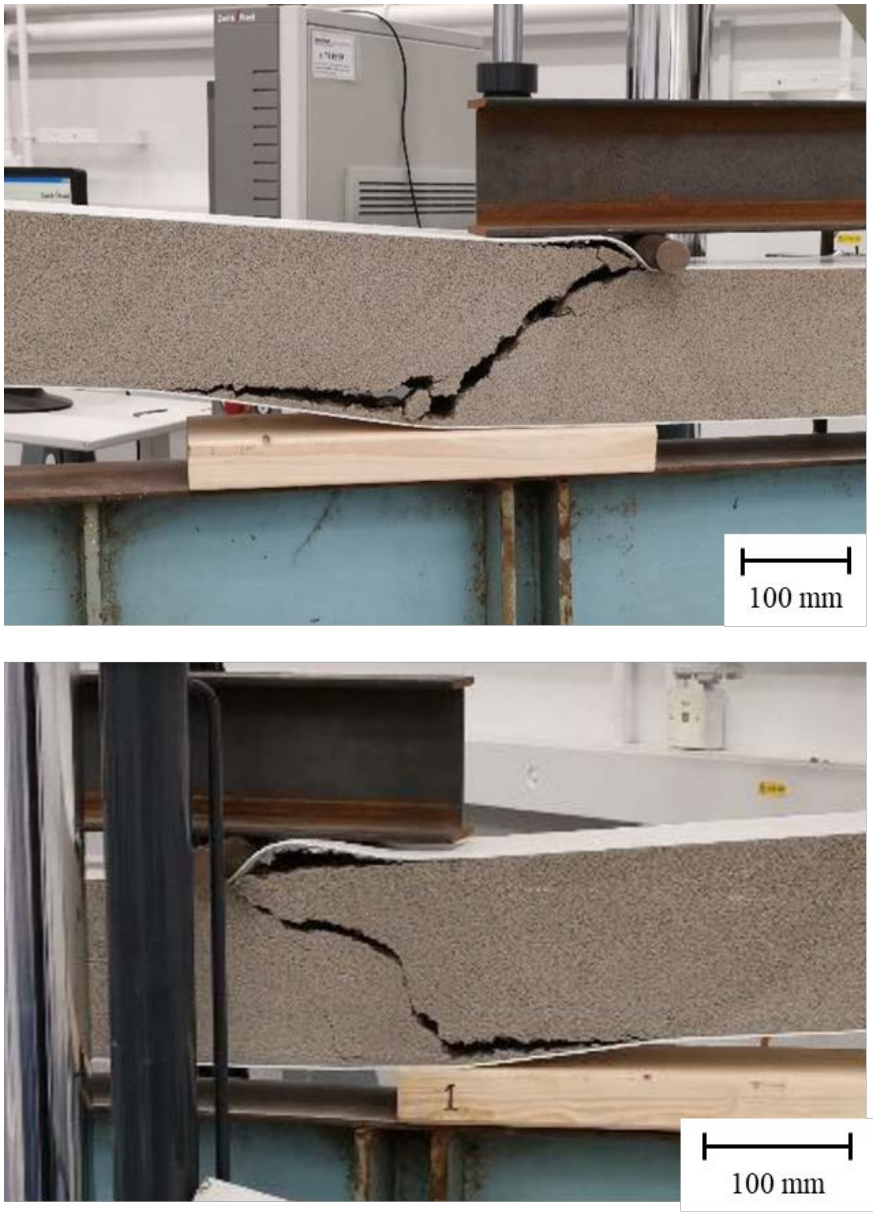

Figure 15: Typical failure modes exhibited in RGBSPs, with longitudinal cracking through a layer of bead core above the adhesive in conjunction with a diagonal shear-induced crack.

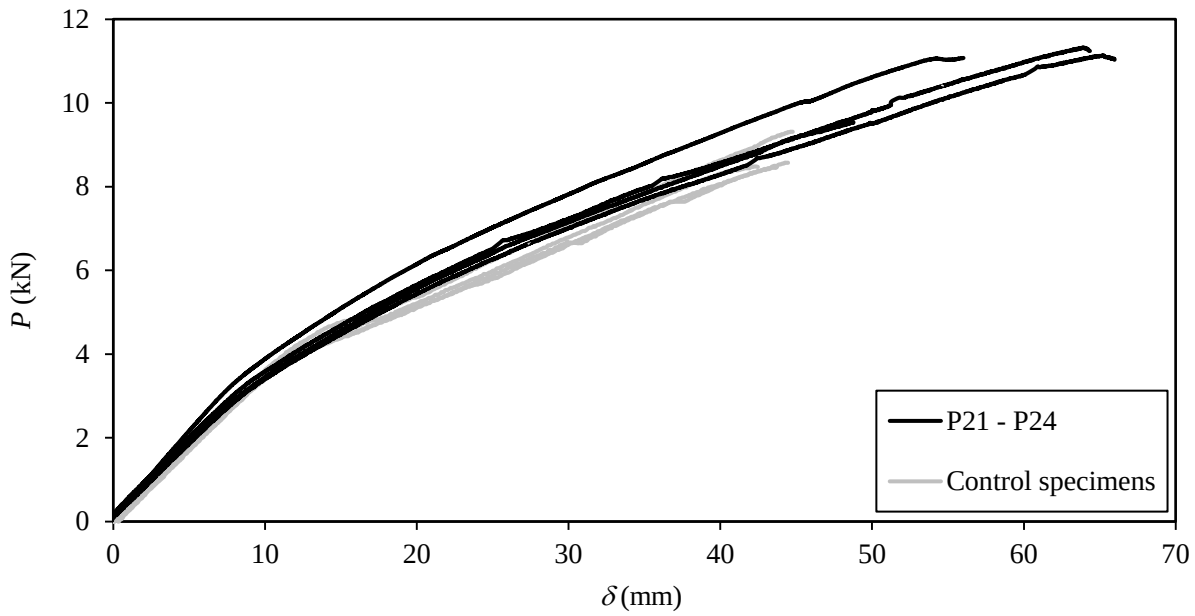

Figure 16: Load–deflection curves of specimens containing additional polyurethane binder compared against those of the control group.

Figure 17: Failure mode observed in specimen P22-1-B150-L2250-XB showing tension side delamination of the facing sheet from the bead core.

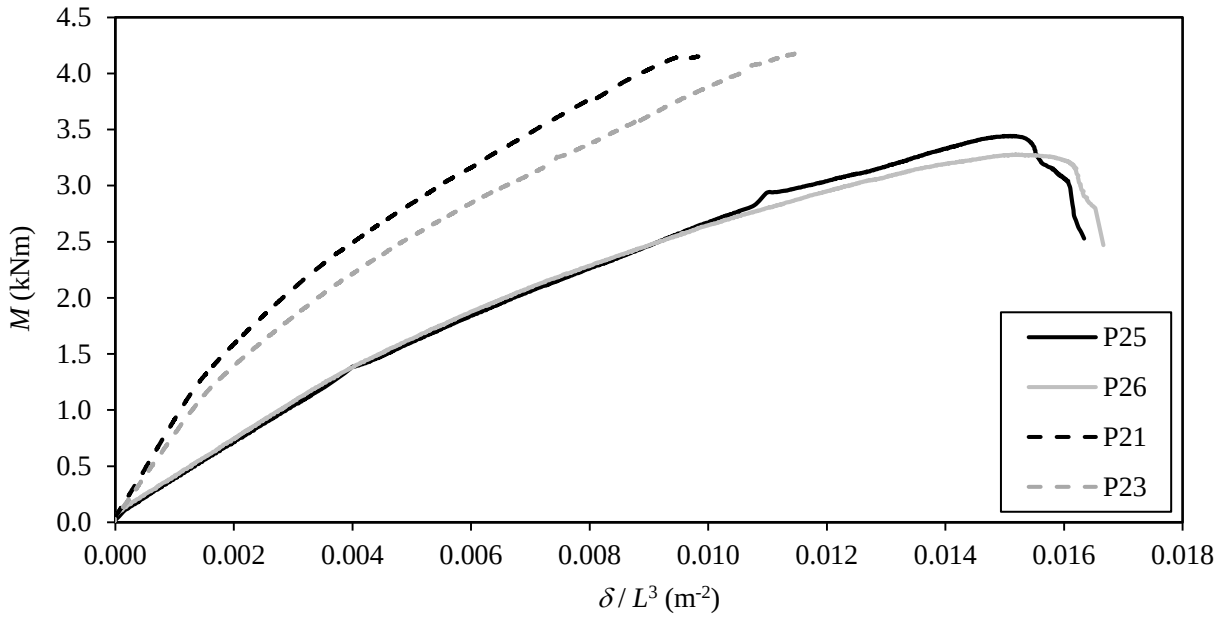

Figure 18: Graphs of applied moment M against δ / L^3 for previously-damaged specimens compared against those of their parent specimens.

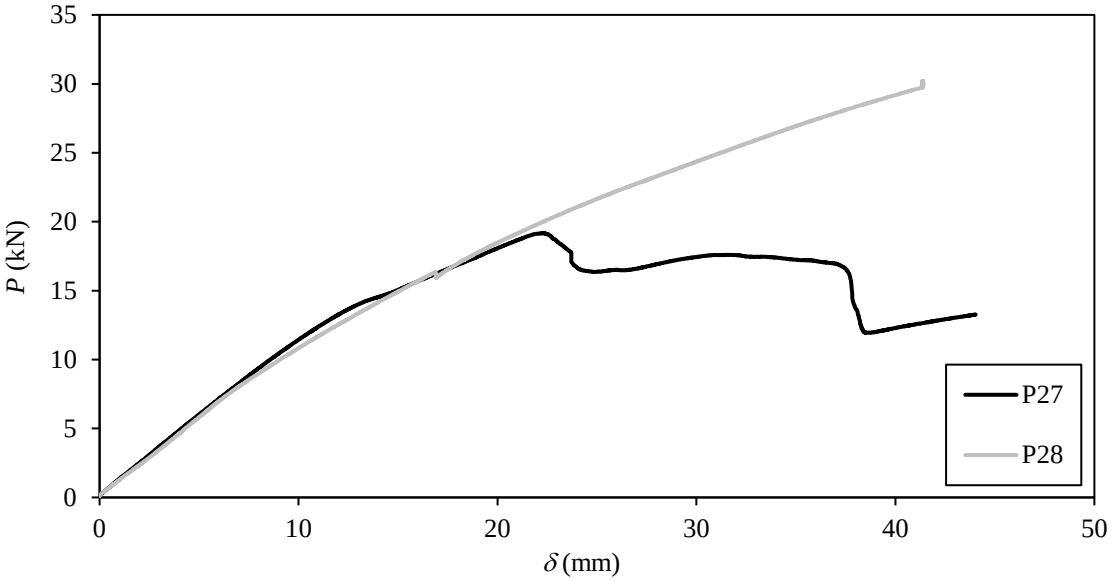

Figure 19: Load–deflection curves of the strain-gauged panels with a nominal width of 450 mm.

a)

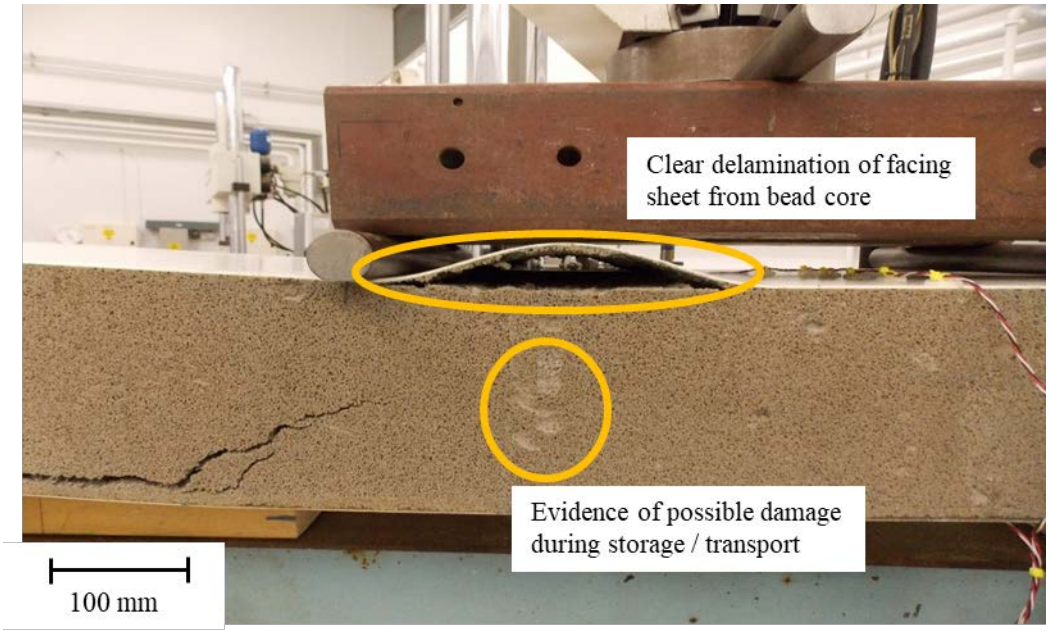

b)

Figure 20: Failure modes observed in a) specimen P27; b) specimen P28.

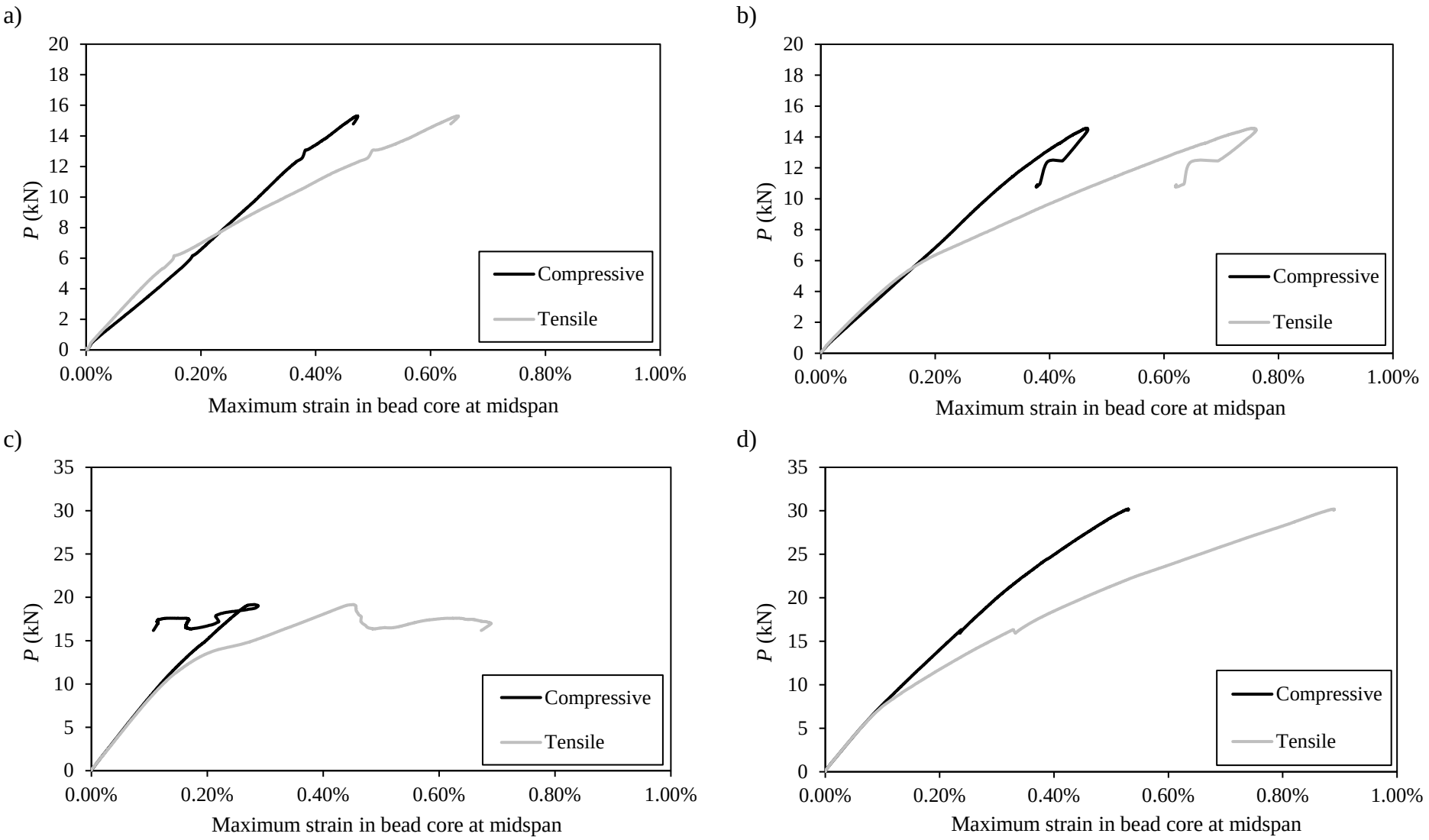

Figure 21: Graphs of load against compressive and tensile strains in the bead core at midspan for a) specimen P25; b) specimen P26; c) specimen P27; d) specimen P28.

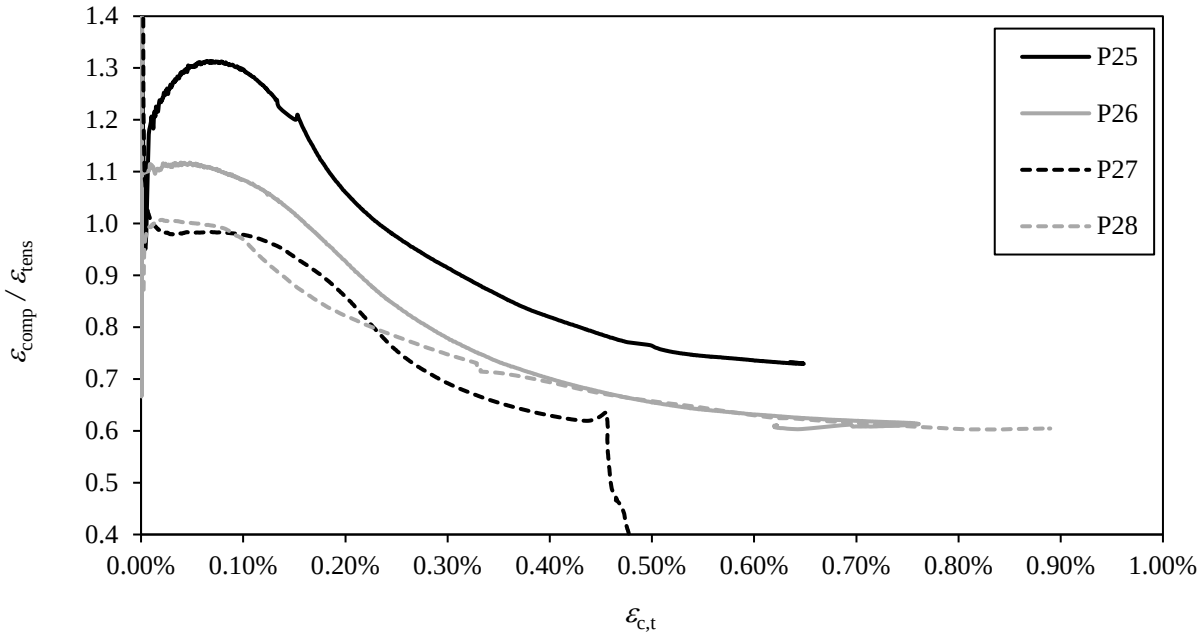

Figure 22: Graphs of ε_{comp} / ε_{tens} against $\varepsilon_{c,t}$ for the strain-gauged specimens.

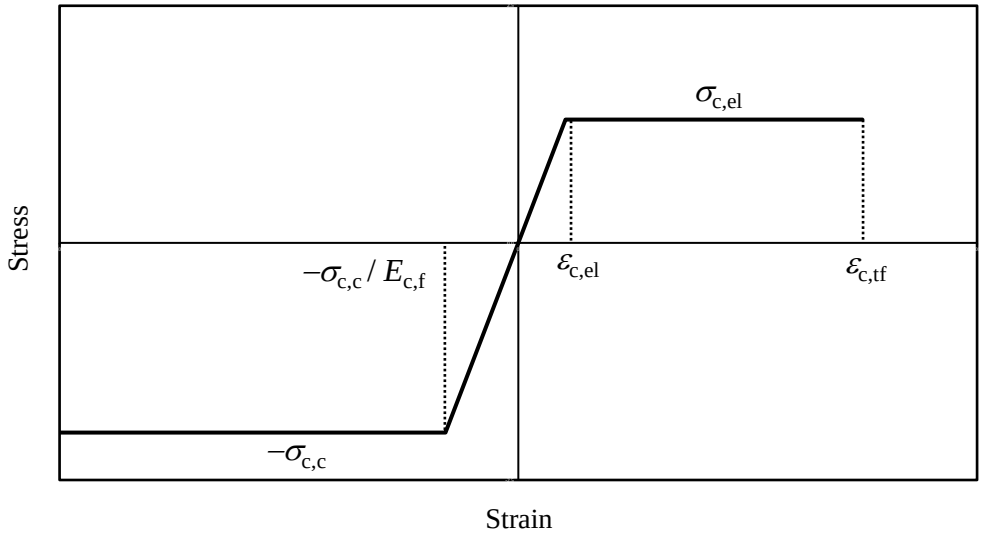

Figure 23: Assumed stress–strain relationship of bead core in tension (positive stress and strain) and compression (negative stress and strain).

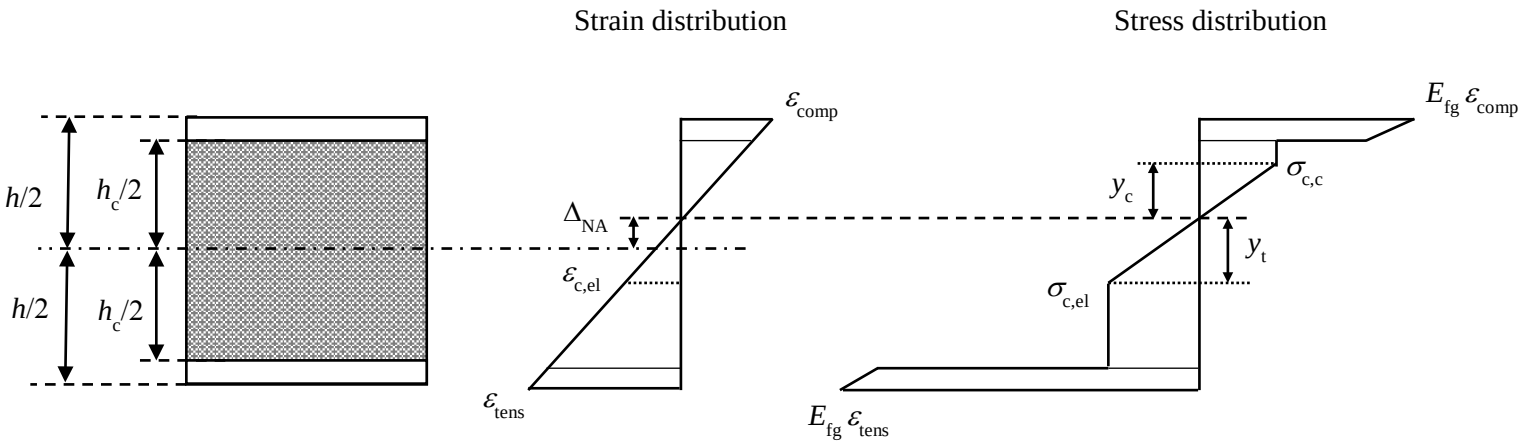

Figure 24: Strain and stress distributions at cross-section undergoing plastic deformation.

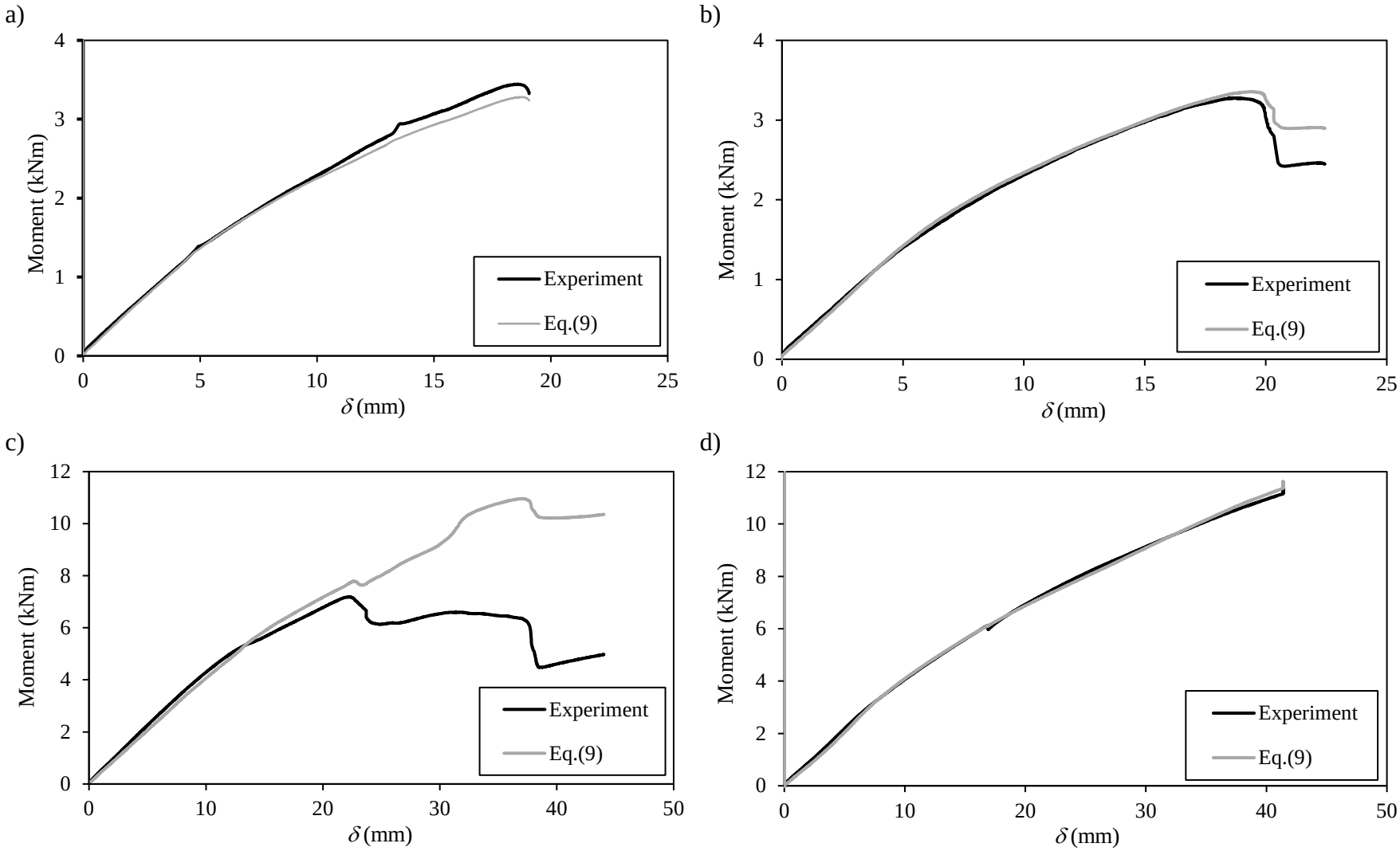

Figure 25: Comparison of experimental and predicted moment–deflection curves for a) specimen P25; b) specimen P26; c) specimen P27; d) specimen P28.

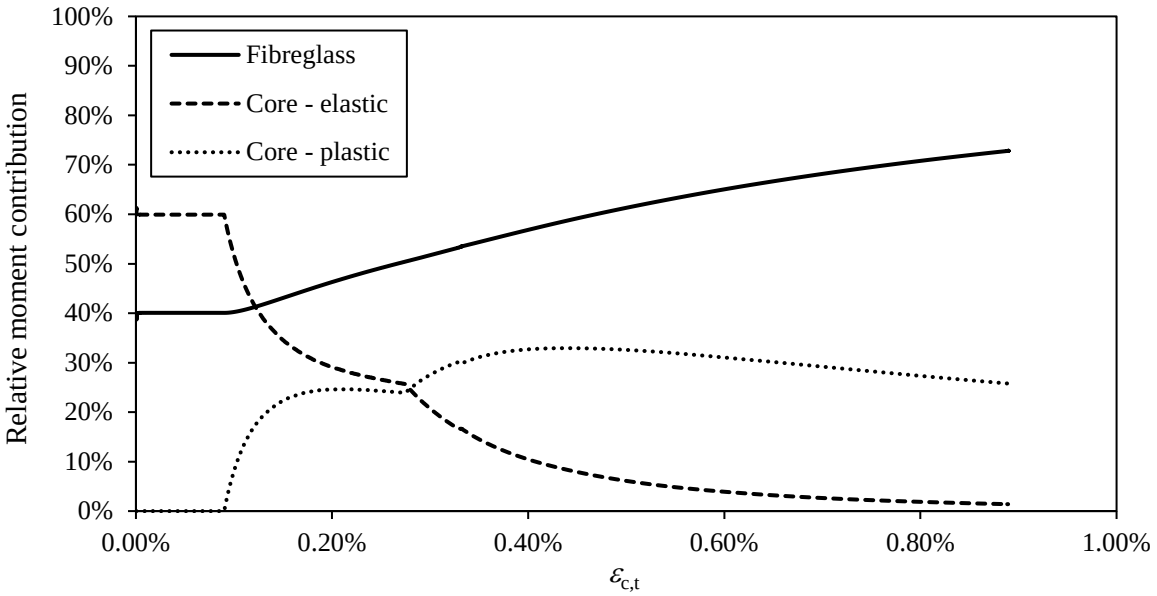

Figure 26: Relative moment contributions of the fibreglass sheets and bead core plotted against the maximum tensile strain in the bead core for specimen P28.

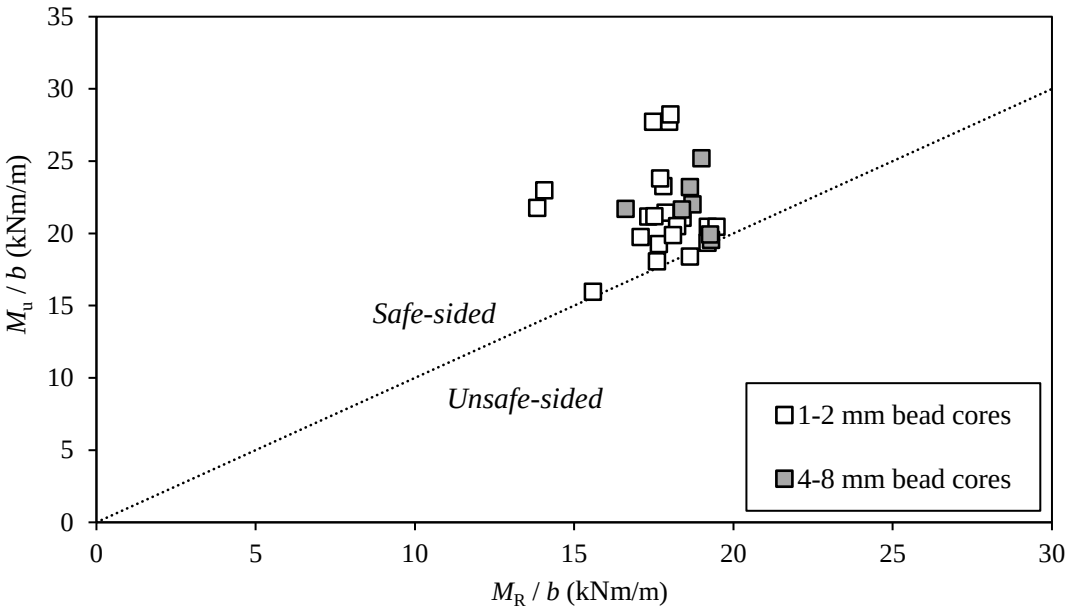

Figure 27: Comparison of experimental and calculated ultimate moments per metre width.

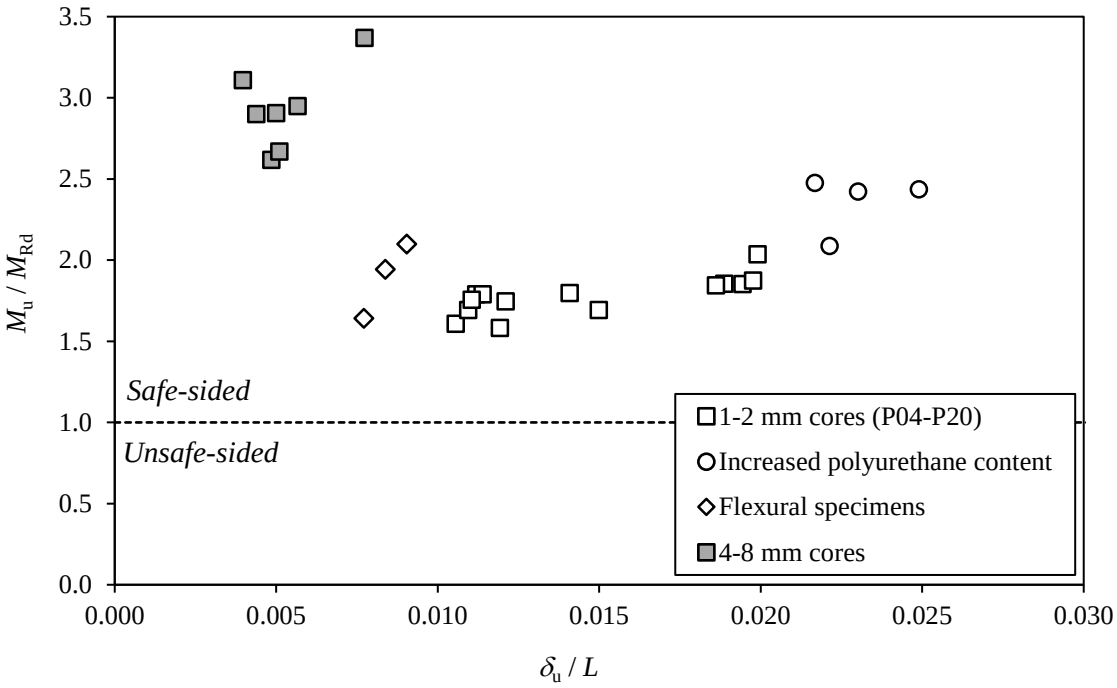

Figure 28: Ratios of experimental to design ultimate resistances.

Table 1: Dimensions and material properties of flexural test specimens.

Specimen	b (mm)	h (mm)	h_c (mm)	t_{fg} (mm)	$E_{c,f}$ (N/mm^2)	$\varepsilon_{c,el}$	$\sigma_{c,el}$ (N/mm^2)
F01	50.32	53.48	48.64	2.42	1312	0.153%	2.00
F02	50.24	52.80	47.74	2.53	993	0.151%	1.50
F03	50.19	54.08	48.76	2.66	1296	0.146%	1.89
- Average	50.25	53.45	48.38	2.54	1201	0.150%	1.80
- COV	0.001	0.012	0.011	0.047	0.150	0.022	0.148

Table 2: Nominal dimensions of RGBSP specimens tested in bending.

	Specimen	Bead diameter range (mm)	Nominal dimensions (mm) $L_{nom} \times b \times h$	L (mm)	a (mm)
Control specimens [14]	P07-1-B150-L1650	1–2	1800 × 150 × 154	1650	550
	P08-1-B150-L1650	1–2	1800 × 150 × 154	1650	550
	P09-1-B150-L1650	1–2	1800 × 150 × 154	1650	550
	P10-1-B150-L1650	1–2	1800 × 150 × 154	1650	550
	P11-1-B150-L2250	1–2	2400 × 150 × 154	2250	750
	P12-1-B150-L2250	1–2	2400 × 150 × 154	2250	750
	P13-1-B150-L2250	1–2	2400 × 150 × 154	2250	750
	P14-1-B150-L2250	1–2	2400 × 150 × 154	2250	750
High-strength adhesive	P17-1-B150-L1650-HSA	1–2	1800 × 150 × 154	1650	550
	P19-1-B150-L1650-HSA	1–2	1800 × 150 × 154	1650	550
	P19-1-B150-L1650-HSA	1–2	1800 × 150 × 154	1650	550
	P20-1-B150-L1650-HSA	1–2	1800 × 150 × 154	1650	550
Increased polyurethane binder	P21-1-B150-L2250-XB	1–2	2400 × 150 × 154	2250	750
	P22-1-B150-L2250-XB	1–2	2400 × 150 × 154	2250	750
	P23-1-B150-L2250-XB	1–2	2400 × 150 × 154	2250	750
	P24-1-B150-L2250-XB	1–2	2400 × 150 × 154	2250	750
Damaged specimens	P25-1-B150-L1350-DM	1–2	1550 × 150 × 154	1350	450
	P26-1-B150-L1350-DM	1–2	1550 × 150 × 154	1350	450
Strain-gauged panels	P27-1-B450-L2000	1–2	2400 × 450 × 154	2000	750
	P28-4-B450-L2000	4–8	2400 × 450 × 154	2000	750

Table 3: Measured dimensions and mechanical properties of RGBSPs tested in the present study.

Specimen	b (mm)	h (mm)	h_c (mm)	t_{fg} (mm)	M_u / b (kNm/m)	δ_u / L^3 (m^{-2})	$E_{c,f}$ (N/mm^2)	$\varepsilon_{c,el}$	$\sigma_{c,el}$ (N/mm^2)
P17-1-B150-L1650-HSA	150.59	153.47	149.17	2.15	19.3	0.00406	958	0.134%	1.29
P18-1-B150-L1650-HSA	150.30	154.54	150.06	2.24	20.5	0.00445	932	0.141%	1.31
P19-1-B150-L1650-HSA	151.44	153.90	149.54	2.18	19.9	0.00455	952	0.144%	1.37
P20-1-B150-L1650-HSA	151.70	154.10	150.10	2.29	19.7	0.00437	968	0.132%	1.28
P21-1-B150-L2250-XB	149.76	152.78	148.40	2.19	27.7	0.00492	1130	0.106%	1.20
P22-1-B150-L2250-XB	150.23	152.60	148.24	2.18	23.8	0.00428	1031	0.118%	1.22
P23-1-B150-L2250-XB	150.64	153.30	149.19	2.06	27.7	0.00579	1047	0.122%	1.28
P24-1-B150-L2250-XB	150.32	153.25	148.97	2.14	28.2	0.00565	1059	0.124%	1.31
P25-1-B150-L1350-DM	149.76	152.78	148.40	2.19	23.0	0.00767	557[1]	0.242%	1.35
P26-1-B150-L1350-DM	150.64	153.30	149.19	2.06	21.8	0.00793	617[1]	0.163%	1.01
P27-1-B450-L2000	450.51	153.73	149.70	2.08	16.0	0.00414	841[1]	0.117%	0.99
P28-4-B450-L2000	449.39	152.94	148.64	2.15	25.2	0.00389	885[1]	0.094%	0.83

[1] Values of $E_{c,f}$ reported for specimens P25–P28 have been obtained using the midspan deflection method for consistency.

Table 4: Elastic properties of bead cores determined using the midspan strain method.

Specimen	$E_{c,f}$ (N/mm^2)		Difference	$\varepsilon_{c,el}$
	Deflection method	Strain method		
P25-1-B150-L1350-DM	557	725	23.2%	0.155%
P26-1-B150-L1350-DM	617	762	19.0%	0.124%
P27-1-B450-L2000	841	1139	26.1%	0.107%
P28-4-B450-L2000	885	1034	14.4%	0.094%

Table 5: Mechanical properties of the bead cores.

	$E_{c,f}$ (N/mm^2)	$\varepsilon_{c,el}$	$\sigma_{c,cc}$ (N/mm^2)
1–2 mm bead cores			
- Average value	1076	0.136%	2.11
- COV	0.10	0.09	0.07
- 5th percentile value	900	0.116%	1.88
4–8 mm bead cores			
- Average value	872	0.104%	2.09
- COV	0.08	0.31	0.11
- 5th percentile value	755	0.051%	1.70

Table 6: Comparison of experimental and predicted ultimate moments.

	Specimen	M_u / b (kNm/m)	M_R / b (kNm/m)	M_u / M_R
Ref.[14]	P01-4-B150-L1650	22.0	18.7	1.18
	P02-4-B150-L1650	19.5	19.3	1.01
	P03-4-B150-L1650	19.9	19.3	1.03
	P04-1-B150-L1650	18.1	17.6	1.03
	P05-4-B150-L2250	21.7	18.4	1.18
	P06-4-B150-L2250	21.7	16.6	1.31
	P07-1-B150-L1650	20.5	19.2	1.07
	P08-1-B150-L1650	18.4	18.6	0.99
	P09-1-B150-L1650	19.3	19.2	1.01
	P10-1-B150-L1650	20.5	19.5	1.05
	P11-1-B150-L2250	21.2	17.5	1.22
	P12-1-B150-L2250	21.4	17.9	1.20
	P13-1-B150-L2250	21.2	17.5	1.21
	P14-1-B150-L2250	23.3	17.8	1.31
	P15-1-B450-L2250	21.1	18.4	1.15
	P16-4-B450-L2250	23.2	18.6	1.25
Present study	P17-1-B150-L1650-HSA	19.3	17.7	1.09
	P18-1-B150-L1650-HSA	20.5	18.2	1.12
	P19-1-B150-L1650-HSA	19.9	18.1	1.10
	P20-1-B150-L1650-HSA	19.7	17.1	1.16
	P21-1-B150-L2250-XB	27.7	18.0	1.54
	P22-1-B150-L2250-XB	23.8	17.7	1.35
	P23-1-B150-L2250-XB	27.7	17.5	1.59
	P24-1-B150-L2250-XB	28.2	18.0	1.57
	P25-1-B150-L1350-DM	23.0	14.1	1.63
	P26-1-B150-L1350-DM	21.8	13.8	1.57
	P27-1-B450-L2000	16.0	15.6	1.02
	P28-4-B450-L2000	25.2	19.0	1.33
	1–2 mm bead cores (all)			
	- Average			1.24
	- COV			0.18
	1–2 mm bead cores (not including P21–P26)			
	- Average			1.11
	- COV			0.09
	4–8 mm bead cores			
	- Average			1.18
	- COV			0.12

Table 7: Parameters and results of the reliability analysis.

Glass bead diameter range	n	b_r	V_δ	V_r	$k_{d,n}$	γ_M
1–2 mm	14	1.12	0.081	0.171	3.62	1.40
4–8 mm	7	1.18	0.105	0.351	3.62	2.20